INSTITUTO SUPERIOR TÉCNICO
Universidade Técnica de Lisboa

Thermal Effects in Interplanetary Spacecraft

The Pioneer Anomaly

Frederico André Branco dos Reis Francisco

Dissertação para a obtenção do Grau de Mestre em

Engenharia Aeroespacial

Júri:

Presidente:	Prof. Doutor Fernando José Parracho Lau (DEM)
Orientador:	Prof. Doutor Paulo Jorge Soares Gil (DEM)
Co-Orientador:	Prof. Doutor Orfeu Bertolami (DF)
Vogal:	Prof. Doutor João Manuel Gonçalves de Sousa Oliveira (DEM)

December 10, 2009

Acknowledgments

To my supervisors for the opportunity to work on this subject and for all their support.

To all my teacher and professors for making it possible for me to get here.

To my family for all the love and care.

To my friends for their presence in all the different moments of my life.

To the one who was at my side. . .

Resumo

Durante as últimas etapas das missões Pioneer 10 & 11, tornou-se evidente a existência de uma aceleração anómala, que ficou conhecida como a Anomalia das Pioneer. A avaliação inicial dos efeitos sistemáticos conhecidos não providenciou uma explicação viável. Desde então, muitos tentaram contabilizá-la através de novos modelos físicos baseados em extensões à Relatividade Geral ou mesmo na sua substituição.

Foram feitas algumas tentativas para explicar a anomalia através de física convencional, nomeadamente através dos efeitos da gravidade da Cintura de Kuiper ou da radiação térmica. Esta última tornou-se objecto de alguma controvérsia, com várias argumentações contra as estimativas iniciais que a descartavam como possível causa da aceleração anómala.

Apresenta-se aqui uma metodologia baseada em fontes de radição pontuais que permite uma estimativa fiável e global da aceleração induzida por efeitos térmicos nas naves Pioneer 10 & 11. Este método foca-se, principalmente, na rapidez de cálculo e na flexibilidade. Foi feita um bateria de casos de teste com vista a avaliar a estabilidade e fiabilidade do método proposto, com resultados bastante satisfatórios.

Os resultados apresentados com base no referido método indicam que os efeitos térmicos são fortes candidatos para a causa da Anomalia das Pioneer. As estimativas produzidas até agora permitem contabilizar entre 35% e 67% da anomalia. Finalmente, aponta-se a via para futuros melhoramentos que ajudarão a refinar estes resultados.

Palavras Chave: Sondas Interplanetárias, Efeitos Térmicos, Pressão de Radiação, Anomalia das Pioneer.

Abstract

During the later stages of the Pioneer 10 & 11 missions, the existence of an anomalous acceleration became evident. This became known as the Pioneer Anomaly. The initial assessment of all known systematic effects provided no explanation. Since then, many have tried to account for it through new physical models based on extensions to General Relativity or even replacing it.

Some attempts to explain the anomaly through conventional physics have been made, namely the gravitation from the Kuiper Belt and thermal effects. The latter have become the object of a heated discussion, with many arguing against the initial estimates that dismissed them altogether as a possible cause of the anomalous acceleration.

We present a methodology based on point-like radiation sources that enables one to perform a reliable and comprehensive estimate of the overall thermally induced acceleration of the Pioneer 10 and 11 spacecraft. This method has its focus on speed and flexibility. A battery of test cases was performed in order to assess the stability and reliability of the proposed method with very satisfactory results.

The results presented based on the aforementioned method indicate that the thermal effects are a strong candidate for the cause of the Pioneer Anomaly. The estimates presented account for 35% to 67% of the anomaly. We also point the way forward indicating future improvements that will help refine these results.

Keywords: Interplanetary Spacecraft, Thermal Effets, Radiation Pressure, Pioneer Anomaly.

Contents

x

List of Figures

List of Tables

List of Acronyms

RTG	Radioisotope Thermoelectric Generator
JPL	Jet Propulsion Laboratory
DSN	Deep Space Network
ODP	Orbital Determination Program
STVG	Scalar-Tensor-Vector Gravity
FEA	Finite Element Analysis
MLI	Multi-Layer Insulation

List of Symbols

Detection of the Anomaly

a_Pio	Sun-ward anomalous acceleration found in the Pioneer Spacecraft
$\Delta\nu$	Frequency shift in Doppler experiments
ν_0	Frequency of the signal emitted from Earth
c	Speed of light
l	Optical distance between the ground station and the spacecraft
ν_model	Modelled return signal frequency
ν_obs	Observed return signal frequency
a_anom	Anomalous acceleration inferred from the frequency residual

Scalar Field Theory

ϕ	Scalar field
$V(\phi)$	Potential of the scalar field
$g_{\nu\mu}$	Metric tensor
$\eta_{\nu\mu}$	Minkowsky metric
$h_{\nu\mu}$	Small perturbation to the metric from the scalar field
$\mathcal{L}_\phi$	Lagrangian density of the scalar field
$T_{\nu\mu}$	Energy-momentum tensor
G	Gravitational constant
T	Trace of the energy-momentum tensor
a_r	Radial acceleration resulting from the scalar field

Scalar-Tensor-Vector Gravity (STVG)

ϕ	STVG Vector field
ω	Vector field coupling strength
μ	Vector field mass
λ	Vector field range
S	Action
g	Determinant of the metric tensor
$\mathcal{L}_\phi$	Lagrangian density of the STVG vector field
$\mathcal{L}_S$	Lagrangian density of the STVG scalar quantities G, ω and μ
$\mathcal{L}_\mathrm{Grav}$	Lagrangian density of gravity
R	Scalar curvature
Λ	Cosmological constant
M	Mass of the central object, *i.e.*, the Sun
ϵ	Charge of the vector particle
J_N	Newtonian orbital angular momentum

Kuiper Belt

a_D	Acceleration due to drag from dust
ρ	Dust density
v_S	Spacecraft velocity relative to the medium
A_S	Spacecraft projected area in the direction of the trajectory relative to the medium
m_S	Spacecraft mass

Radiation Pressure

$\vec{S}$	Poynting vector
$\vec{E}$	Electric field
$\vec{H}$	Magnetic induction field
$\vec{D}$	Electric displacement
$\vec{B}$	Magnetic field
u_em	Energy density of the electromagnetic field
$\vec{J}$	Current density
ε	Electric permitivity of the medium
μ	Magnetic permeability of the medium
$\vec{k}$	Direction of wave propagation (unitary vector)
v	Wave propagation velocity
c	Wave propagation velocity in the vacuum (speed of light)
P_rad	Radiation pressure
α	Radiation pressure coefficient
$\vec{n}$	Surface normal
E_γ	Energy carried by a photon
h	Planck's constant
ν_γ	Photon frequency
E	Energy
m_0	Rest mass
p	Linear momentum
A	Area of the exposed surface

Point-like source method

W	Emitted power
I	Optical intensity
$\vec{G}$	Parameterisation of the illuminated surface
$\vec{F}_\mathrm{rad}$	Force due to radiation
$\vec{a}_\mathrm{Th}$	Acceleration due to thermal radiation
m	Vehicle mass

Power budget

$\dot{E}_\mathrm{absorb}$	Power absorbed from the medium
$\dot{E}_\mathrm{gen}$	Power generated onboard
A_i	Surface area
ϵ_i	Surface emissivity
σ	Stefan-Boltzmann constant
T_i	Surface absolute temperature

Chapter 1

Introduction

1.1 General Background

1.1.1 The Pioneer Anomaly

Long-range spacecraft provide a unique opportunity to carry out celestial mechanics and gravitation experiments. The Pioneer 10 & 11 deep-space probes are the manmade objects with the greatest orbital determination accuracy and are especially suited for this kind of study.

The Pioneer 10 & 11 were launched in the early 1970's as part of NASA's Pioneer program of planetary exploration. The Pioneer 10 was launched from Cape Canaveral on March 3, 1972 heading for Jupiter. Its sister ship, the Pioneer 11, followed suit about a year later on April 6, 1973 and would become the first mission to explore Saturn.

The spacecraft for these missions, depicted in Fig. 1.1, were built around a central compartment containing all the equipment and scientific instrumentation. Behind the main compartment, there is the $2.74 \mathrm{~m}$ diameter high-gain antenna that always faces Earth. Extending from the main compartment, there are two trusses $120°$ apart, each holding a Radioisotope Thermoelectric Generator (RTG) at approximately $3 \mathrm{~m}$ from the centre of the spacecraft, as shown in Fig. 1.1. These RTGs are responsible for onboard power generation.

As they were supposed to be the first human spacecraft to travel beyond our Solar system, both probes also carried a plaque, shown in Fig. 1.2, containing a depiction of male and female human beings, the probe itself and a navigational chart with the location of Earth with respect to several known pulsars [1].

The Pioneer 10 & 11 missions provided invaluable scientific data from their visits to Jupiter and Saturn, including some of the first close up photographs of these planets, like those in Figs 1.3 & 1.4. Among their scientific objectives were the study of the interplanetary and planetary magnetic fields, solar wind parameters, cosmic rays, transition region of the heliosphere, neutral hydrogen abundance, and the atmosphere of Jupiter, Saturn and some of their satellites [1].

The Pioneer 10 would become the first manmade object to cross the asteroid belt and, by some definitions, to leave the solar system. The last contact of the Pioneer 10 with Earth was on January 23, 2003, from more than $80 \mathrm{~AU}$ away [1]. The two Pioneer probes currently follow hyperbolic trajectories away from the Solar System in approximately opposite directions. The success of these missions would pave the way for the heavier and more advanced Voyager 1 & 2 missions a few years later, that would repeat the visits to Jupiter and Saturn and be the first to make Uranus and Neptune fly-bys.

Through the later stages of the Pioneer missions, the analysis of the radiometric data began to reveal the presence of an anomalous acceleration. The existence of this acceleration, that became known as the Pioneer Anomaly, was first put forward by Anderson *et al.* [7] and later verified through independent methods by Markwardt [8] and Toth [9]. With the subsequent availability of new data sets more detailed analyses carried
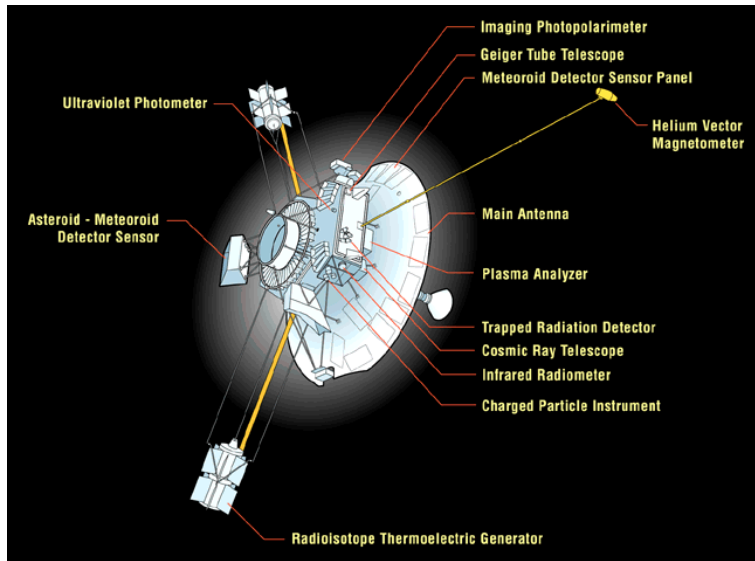
Figure 1.1: Schematic of the Pioneer 10 & 11 spacecraft configuration, taken from Ref. [1]. Here are visible the main equipment compartment, high-gain antenna and RTGs.
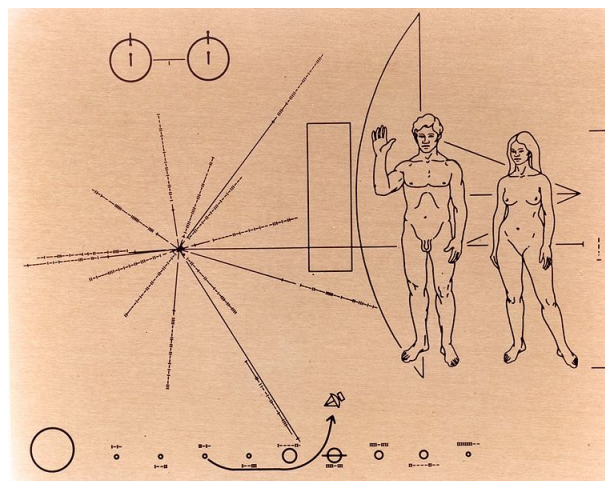
Figure 1.2: Depiction of the plaque carried aboard the Pioneer 10 & 11 probes in an attempt to make contact with any extraterrestrial species that could eventually encounter the probe.

Figure 1.3: Pioneer 10 photograph of Jupiter.
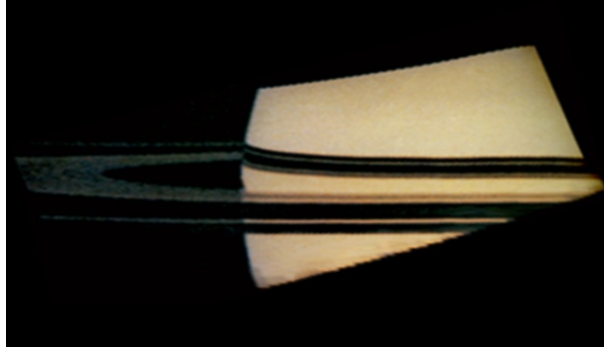
Figure 1.4: Pioneer 11 photograph of Saturn.

out by the team led by the Jet Propulsion Laboratory (JPL) achieved a final value of $a_{\mathrm{Pio}} = (8.74 \pm 1.33) \times 10^{-10}$ m/s^2 [2].

Since then, many possible explanations for this phenomenon have been put forward. There was an initial attempt to account for all systematic effects that failed to provide a credible cause, raising the possibility of a previously unknown fundamental physical effect [2]. This set the stage for the Pioneer Anomaly to acquire great relevance as a test to General Relativity.

More recently, however, the issue of thermal effects has been once again raised as a possible explanation for the anomalous acceleration of the Pioneer probes. The purpose of this work is to provide a careful and systematic analysis of the physics involved in the thermal radiation and develop a method to compute its influence on the trajectories of interplanetary spacecraft. Specifically, the case of the Pioneer spacecraft is the object of attention in the context of the aforementioned anomalous acceleration. This dissertation reports on the work developed and results published in Ref. [10].

1.1.2   Detection and Characterisation of the Anomaly

An extensive study about the Pioneer Anomaly is presented in Ref. [2], including data collection and treatment as well as an evaluation of the main sources of systematic error. In order to establish some background on the subject, a brief summary of that work is presented in this section.

Communications with deep space probes like the Pioneer 10 & 11 are carried out through the antennas of the three ground stations of the Deep Space Network (DSN). These installations are located in California, Spain and Australia, providing an integral coverage of the sky. The infrastructure of the DSN allows for a frequency accuracy of at least 10^{-12}. This allows the DSN to be used in the process of position and trajectory determination of interplanetary spacecraft like the Pioneer probes, involving three different sets of measurements.

Doppler experiments are performed through the DSN by transmitting a signal to the spacecraft that is coherently transponded upon reception and transmitted back to Earth. The frequency shift $\Delta\nu$ is measured and used to determine the time derivative of the optical distance l or a "range rate" through

$$\Delta\nu(t) = \nu_0 \frac{1}{c}\frac{dl}{dt}, \tag{1.1}$$

where ν_0 is the initial frequency of the signal transmitted from Earth and c is the speed of light.

The range is measured using a phase modulated signal in the carrier wave of the up-link. This signal is received, demodulated, filtered and re-modulated onto the down-link. Upon reception of the returned signal, its phase is compared with the outgoing signal and the range is inferred with the help of an Orbit Determination Program (ODP).

The position of the spacecraft in the sky can be extracted from the Doppler data by examining the diurnal
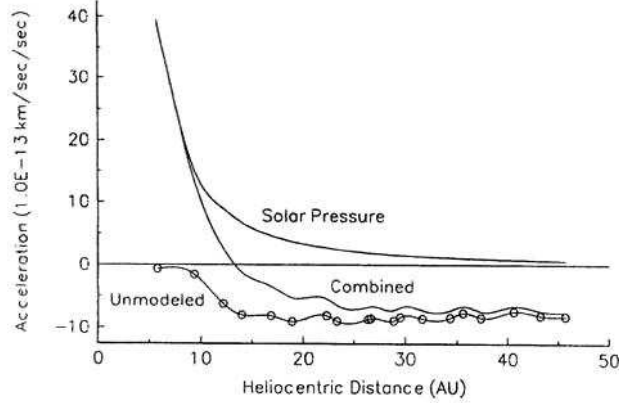
Figure 1.5: ODP plots of accelerations on Pioneers 10/11 as a function of distance from the Sun, taken from Ref. [2]. The accelerations are the calculated solar radiation acceleration (top line), the unmodelled acceleration (bottom line) and the sum of the two above (middle line).

variation in the Doppler shift caused by the Earth's rotation. The Doppler shift data will appear modulated as a sinusoid with an amplitude dependent on the declination angle of the spacecraft and its phase dependent on the right ascension. These angles can therefore be estimated from the Doppler shift record. Furthermore, using ODPs, through the dynamics of spacecraft motion, a calculation for the range can also be performed from these measurements.

These three independent sets of data are all complementary and provide the tools to establish the position and speed of the Pioneer probes. This is done with ODPs that provide a modelled value for the parameters not directly measurable, in particular, the acceleration. The codes used for this purpose include the effects of planetary perturbations, solar radiation pressure, the interplanetary medium, general relativity, together with bias and drift in the Doppler signal.

An expected frequency for the return signal can be derived from the modelled acceleration. The comparison between the modelled frequency $\nu_{\mathrm{model}}(t)$ and the one observed in the DSN antennas $\nu_{\mathrm{obs}}(t)$ will indicate the existence of any unmodelled or anomalous acceleration $a_{\mathrm{anom}}(t)$. This effect will appear as a frequency residual

$$\nu_{\mathrm{model}}(t) - \nu_{\mathrm{obs}}(t) = \left(1 - \frac{2\, a_{\mathrm{anom}}(t)\, t}{c}\right). \tag{1.2}$$

The search for unmodelled accelerations began in 1980 for the Pioneer 10, which was by then approximately 20 AU away. At this point, the acceleration due to solar radiation pressure is lower than 5×10^{-10} m/s^2. Initial studies indeed revealed the presence of an anomalous acceleration with its main observational signature being an apparently constant acceleration directed towards the Sun with a value of $(8 \pm 3) \times 10^{-10}$ m/s^2. This acceleration is shown in Fig. 1.5, appearing as soon as the Sun's radiation influence becomes less significant.

Attempts were made from the outset to explain this bias with eventual perturbative forces like the Kuiper belt's gravity, galaxy's gravity, gas leaks from spacecraft, errors in the planetary ephemeris, and errors in the accepted values of the Earth's orientation, precession, and nutation. None of these mechanisms turned out to be a credible candidate to explain this anomaly, while others like heat radiation were ruled out from the beginning.

Further analysis of the data allowed the JPL led team to obtain a more accurate characterisation of the anomalous acceleration. The obtained values were $(8.09 \pm 0.21) \times 10^{-10}$ m/s^2 for the Pioneer 10 and $(8.56 \pm 0.15) \times 10^{-10}$ m/s^2 for the Pioneer 11. There is no statistically significant magnitude variation with distance between 40 and 60 AU up to a sensitivity of 2×10^{-10} m/s^2.

A comprehensive attempt to account for all systematic sources of error that could explain the anomalous

Table 1.1: Error budget for the Pioneer 10 and 11, taken from Ref. [2].

Item	Description of error budget constituents	Bias (10^{-8} cm/s^2)	Uncertainty (10^{-8} cm/s^2)
1	Systematics generated external to the spacecraft:		
	a) Solar radiation pressure and mass	+0.03	±0.01
	b) Solar wind		$\pm < 10^{-5}$
	c) Solar corona		±0.02
	d) Electro-magnetic Lorentz forces		$\pm < 10^{-4}$
	e) Influence of the Kuiper belt's gravity		±0.03
	f) Influence of the Earth orientation		±0.001
	g) Mechanical and phase stability of DSN antennae		$\pm < 0.001$
	h) Phase stability and clocks		$\pm < 0.001$
	i) DSN station location		$\pm < 10^{-5}$
	j) Troposphere and ionosphere		$\pm < 0.001$
2	On-board generated systematics:		
	a) Radio beam reaction force	+1.10	±0.11
	b) RTG heat reflected off the craft	−0.55	±0.55
	c) Differential emissivity of the RTGs		±0.85
	d) Non-isotropic radiative cooling of the spacecraft		±0.48
	e) Expelled Helium produced within the RTGs	+0.15	±0.16
	f) Gas leakage		±0.56
	g) Variation between spacecraft determinations	+0.17	±0.17
3	Computational systematics:		
	a) Numerical stability of least-squares estimation		±0.02
	b) Accuracy of consistency/model tests		±0.13
	c) Mismodeling of maneuvers		±0.01
	d) Mismodeling of the solar corona		±0.02
	e) Annual/diurnal terms		±0.32
	Estimate of total bias/error	+0.90	±1.33

acceleration resulted in the production of Table 1.1. The error sources are divided into systematics external to the spacecraft, internal spacecraft systematics and computational errors. The table gives an estimate of the bias and error budget introduced by each of the considered effects. After adding this bias and error budget to the previous estimates of the acceleration one arrives at the final value for the anomalous acceleration presented in Ref. [2]:

$$a_{\mathrm{Pio}} = (8.74 \pm 1.33) \times 10^{-10} \text{ m/s}^2. \tag{1.3}$$

This analysis, however, does not rule out a non-constant acceleration. For example, an effect characterised by a linear decay with a time constant larger than 50 years also produces a residual signature that is compatible with the telemetry. Furthermore, due to the distances involved, the data is not accurate enough to constrain whether the anomalous acceleration is geocentric or heliocentric [8]. Ascertaining this would provide relevant insight concerning the origin of the anomaly.

1.2 Possible Explanations

1.2.1 New Physics

With the apparent failure of all known conventional effects to explain the Pioneer Anomaly, the initial work by Anderson *et al.*, summarised in Section 1.1.2, raised the question if there was a fundamentally physical origin to it. Several theories have been put forward, either presenting new manifestations of already known physics or with entirely new theories modifying or replacing General Relativity (A comprehensive list of these proposals can be found on Ref. [11]).

To illustrate the kind of proposals made in this field, a brief description of two of these models is presented.

Scalar Field

One possible way to look at this problem is in the context of a braneworld scenario, as done by Bertolami & Páramos in Ref. [11]. In braneworld theories, our Universe is assumed to be a 3-dimensional membrane embedded in a higher dimensional bulk space.

The work summarised here uses a Randall-Sundrum braneworld model and tries to explain the Pioneer Anomaly as an influence of the radion field, a scalar perturbation of the metric related to relative motion of the two branes. The authors conclude that this approach is unsuitable to provide the desired explanation [11].

However, a possible explanation for the Pioneer anomalous acceleration can arise from the presence of a scalar field ϕ with a potential $V(\phi) \propto -\phi^{-\alpha(r)}$ with $\alpha > 0$. This field is similar to the form a supergravity inspired quintessence field assumes in braneworld theories, although with the sign reversed.

The effect appears in the metric $g_{\mu\nu}$ as a small perturbation $h_{\mu\nu}$ to the Minkowsky metric $\eta_{\mu\nu}$:

$$g_{\mu\nu} = \eta_{\mu\nu} + h_{\mu\nu}. \tag{1.4}$$

The Lagrangian density $\mathcal{L}_\phi$ of the scalar field takes the form

$$\mathcal{L}_\phi = \frac{1}{2}\eta_{\mu\nu}\partial_\mu\phi\partial^\nu\phi - V(\phi). \tag{1.5}$$

Since this is a spherically symmetric problem, the formulation can be developed in spherical coordinates. Hence, Eq. (1.5) takes the form

$$\mathcal{L}_\phi = \frac{1}{2}\eta_{rr}(\phi')^2 - A^2\phi^{-\alpha}, \tag{1.6}$$

where A is a constant. The equation of motion of the scalar field is

$$\Box^2\phi + \frac{dV(\phi)}{d\phi} = 0, \tag{1.7}$$

where $\Box = \partial_\mu\partial^\mu$ is the d'Alembertian operator. This equation has as a solution in spherical coordinates

$$\phi(r) = \left((2+\alpha)\sqrt{\frac{\alpha}{8+\alpha}}Ar\right)^{\frac{2}{2+\alpha}} \equiv \beta^{-1}r^{\frac{2}{2+\alpha}}. \tag{1.8}$$

This means that the potential takes the form

$$V(\phi(r)) = -A^2\beta^\alpha r^{\frac{2}{2+\alpha}}, \tag{1.9}$$

while the gradient term becomes

$$\frac{1}{2}(\phi'(r))^2 = A\left(\frac{\alpha}{4+\alpha}\right)\beta^\alpha r^{-\frac{2\alpha}{2+\alpha}}. \tag{1.10}$$

The Lagrangian density in the Newtonian limit is given by

$$\mathcal{L}_\phi = -\frac{4}{4+\alpha} V(\phi). \tag{1.11}$$

The energy-momentum tensor for the scalar field is given by the expression

$$T_{\mu\nu} = \partial_\mu \phi \partial_\nu \phi - \eta_{\mu\nu} \mathcal{L}_\phi. \tag{1.12}$$

This is then introduced in the linearised form of Einstein's equation

$$\frac{1}{2} \nabla^2 h_{\mu\nu} = 8\pi G \left(T_{\mu\nu} - \frac{1}{2} \eta_{\mu\nu} T \right), \tag{1.13}$$

where G is the gravitational constant. From the solution of this equation, one can obtain the radial acceleration caused by the scalar field

$$a_r = -\frac{C}{r^2} + (2+\alpha) A^2 8\pi G \beta^\alpha r^{-\frac{2\alpha}{2+\alpha}} \left(\frac{C}{2} - \frac{r}{6+\alpha} \right), \tag{1.14}$$

where C is a constant.

For $\alpha = 2$ one gets an expression for the acceleration that is compatible with the main constant observational signature of the Pioneer Anomaly:

$$a_r = -\frac{C}{r^2} + \sqrt{\frac{3}{2}} A^2 2\pi G + \sqrt{\frac{3}{2}} \frac{AC 8\pi G}{r}. \tag{1.15}$$

The first term represents the Newtonian contribution and the term proportional to r^{-1} is much smaller than the constant term for $4C/r \ll 1$, that is for $r \gg 6$ km, and is also much smaller than the Newtonian acceleration for $r \ll 2.9 \times 10^{22}$ km ≈ 100 Mpc, clearly covering the desired range. The constant term can, therefore, be identified with the anomalous acceleration by setting the constant A appropriately. If $a_{\mathrm{Pio}} = 8.5 \times 10^{-10}$ m/s^2 then $A = 4.7 \times 10^{-10}$ m/s^2 [11].

Scalar-Tensor-Vector Gravity

Another proposal was put forward by Brownstein & Moffat using Scalar-Tensor-Vector Gravity (STVG) theory to obtain an effect that fits the available data. The theory is outlined in Refs. [12, 3] and postulates the existence of a spin -1 vector field ϕ. Furthermore, in this theory the gravitational constant G, the vector field coupling strength ω and the vector field mass $\mu = 1/\lambda$ are all treated as scalar fields with their own dynamics. The action for STVG takes the form

$$S = \int dx^4 \sqrt{-g} (\mathcal{L}_{\mathrm{Grav}} + \mathcal{L}_\phi + \mathcal{L}_S), \tag{1.16}$$

where g is the determinant of the metric. This action includes the Lagrangian densities for the vector field

$$\mathcal{L}_\phi = \omega \left(\frac{1}{4} (\partial^\mu \phi^\nu - \partial^\nu \phi^\mu)(\partial_\mu \phi_\nu - \partial_\nu \phi_\mu) + V(\phi) \right), \tag{1.17}$$

for the scalar quantities G, ω and μ

$$\mathcal{L}_S = \frac{1}{G^3}\left(\frac{1}{2}g^{\mu\nu}\nabla_\mu G\nabla_\nu G + V(G)\right) +$$
$$+\frac{1}{G}\left(\frac{1}{2}g^{\mu\nu}\nabla_\mu\omega\nabla_\nu\omega + V(\omega)\right) +$$
$$+\frac{1}{\mu^2 G}\left(\frac{1}{2}g^{\mu\nu}\nabla_\mu\mu\nabla_\nu\mu + V(\mu)\right) \tag{1.18}$$

and for gravitation

$$\mathcal{L}_{\text{Grav}} = \frac{1}{16\pi G}(R + 2\Lambda), \tag{1.19}$$

where R is the scalar curvature and Λ is the cosmological constant.

From the development of the field equations, the equations of motion for a static spherically symmetric field about a central mass M can be obtained. The line element is written in spherical coordinates as

$$ds^2 = \gamma(r)dt^2 - \alpha(r)dr^2 - r^2(d\theta^2 + \sin^2\theta d\varphi^2). \tag{1.20}$$

An exact solution for the spherically symmetric static field equations can be obtained if the potential $V(\phi)$ and Λ are small enough to be neglected, yielding

$$\gamma(r) = 1 - \frac{2GM}{r} + \frac{Q^2}{r^2} \; , \;\; \alpha(r) = 1 - \frac{2GM}{r} + \frac{Q^2}{r^2}, \tag{1.21}$$

where the charge ϵ of the spin -1 vector particle is taken into account in the quantity

$$Q = 4\pi G\omega\epsilon^2. \tag{1.22}$$

That can be compared to the usual Schwarzschild solution

$$\gamma_{\text{Schwarz}}(r) = 1 - \frac{2GM}{r} \; , \;\; \alpha_{\text{Schwarz}}(r) = \frac{1}{1 - \frac{2GM}{r}}. \tag{1.23}$$

We can easily see that, as expected, for large values of r the STVG solution degenerates in the Schwarzschild solution. With some more manipulation, described in detail in Ref. [12], we finally obtain the equation of motion of a particle around a mass M

$$\frac{d^2 r}{dt^2} - \frac{J_N^2}{r^3} + \frac{GM}{r^2} = K\frac{e^{-\mu r}}{r^2}(1 + \mu r). \tag{1.24}$$

where J_N is the Newtonian orbital angular momentum and K is a positive quantity. Following the formulation developed in Ref. [3], the radial acceleration can be written as

$$a(r) = -\frac{G_\infty M}{r^2} + K(r)\frac{e^{-r/\lambda(r)}}{r^2}\left(1 - \frac{r}{\lambda(r)}\right). \tag{1.25}$$

The value for the gravitational constant appears renormalized as

$$G_\infty = G_0\left(1 + \alpha_\infty\right), \tag{1.26}$$

where G_0 here denotes the usual newtonian gravitational constant. The value for K is chosen as

$$K(r) = G_0 M\alpha(r). \tag{1.27}$$

8

Using Eq. (1.27), we can finally write the variation of G with distance to the central mass

$$G(r) = G_0 \left[1 + \alpha(r) \left[1 - e^{-r/\lambda(r)} \left(1 - \frac{r}{\lambda(r)} \right) \right] \right] \qquad (1.28)$$

and the acceleration

$$a(r) = -\frac{G(r)M}{r^2}. \qquad (1.29)$$

The authors then postulate that the Pioneer Anomaly is caused by the difference between the Newtonian gravitational constant G_0 and the new dynamic value $G(r)$. The anomalous Pioneer acceleration would thus be given by

$$a_{\mathrm{Pio}} = -\frac{\Delta G(r) \, M_\odot}{r^2}, \qquad (1.30)$$

where

$$\Delta G(r) = G(r) - G_0 = G_0 \left[\alpha(r) \left[1 - e^{-r/\lambda(r)} \left(1 - \frac{r}{\lambda(r)} \right) \right] \right]. \qquad (1.31)$$

The proposed parametric representations for $\alpha(r)$ and $\lambda(r)$ are:

$$\alpha(r) = \alpha_\infty (1 - e^{\frac{r}{\bar{r}}})^{\frac{b}{2}}, \qquad (1.32)$$

$$\lambda(r) = \frac{\lambda_\infty}{(1 - e^{\frac{r}{\bar{r}}})^b}. \qquad (1.33)$$

Here, $\bar{r}$ is a non-running distance scale parameter and b is a constant.

Using a least-squares routine, the authors obtain values for the constant parameters that yield the best fit to the acceleration residuals:

$$\alpha_\infty = (1.00 \pm 0.02) \times 10^{-3},$$
$$\lambda_\infty = 47 \pm 1 \, \mathrm{AU},$$
$$\bar{r} = 4.6 \pm 0.2 \, \mathrm{AU},$$
$$b = 4.0.$$

The graph in Fig. 1.6 plots the obtained prediction for the anomalous acceleration compared with the data from both Pioneer probes.

Finally, the authors argue that the STVG theory can explain the anomalous acceleration and still be consistent with the equivalence principle, lunar laser ranging and satellite data for the inner solar system as well as the outer solar system planets [3].

1.2.2 The Kuiper Belt

One of the initial candidates to explain the Pioneer Anomaly was the gravitational effect of the Kuiper belt. A detailed approach to the influence of the Kuiper belt's gravity was carried out by Bertolami & Vieira, considering several different models for the mass distribution [4].

The analysed models were a two ring model, a uniform disk, a non-uniform disk and a uniform torus model. The two ring and uniform disk models had been previously analysed in Ref. [2], placing a limit of
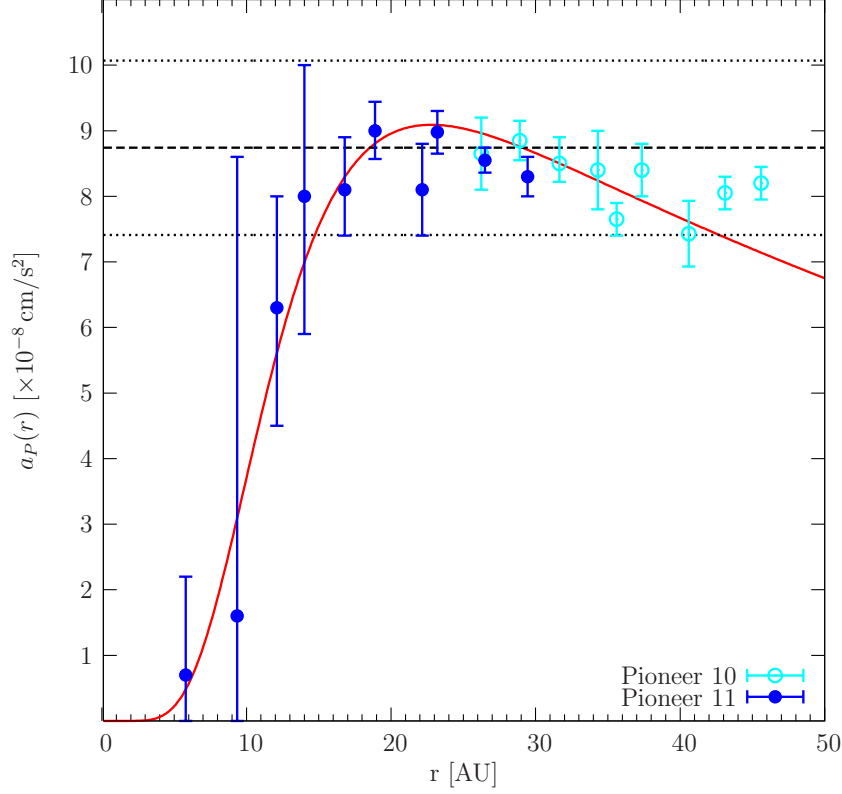
Figure 1.6: Best fit to the Pioneer anomalous acceleration data plotted against the position, r in AU, on a linear scale out to $r = 50$ AU, as presented in Ref. [3].

$\pm 0.03 \times 10^{-10}$ m/s^2, as shown in Table 1.1.

In Ref. [4], the radial acceleration is computed for each model, with the results shown in Fig. 1.7. The Kuiper Belt's mass is set at $M_{\mathrm{KB}} = 0.3 M_{\mathrm{Earth}}$, the maximum allowed by the far-infrared emission observations.

In all of the models the acceleration changes from Sun-ward positive to negative between 30 and 40 AU. The non-uniform disk models yields the result closest to the constant acceleration that is the main observational signature of the Pioneer Anomaly.

Despite that, the values are always much lower than the effect observed on the Pioneer spacecraft. The highest acceleration obtained is 0.064×10^{-10} m/s^2, which is 0.73% of the Pioneer Anomaly. Still, it is around double the maximum value previously admitted for this effect [2].

After ruling out gravitational acceleration from the Kuiper Belt, the effect of drag from interplanetary dust was assessed.

Drag induced acceleration can be modelled as

$$a_{\mathrm{D}}(r) = -\frac{\rho(r) v_{\mathrm{s}}(r)^2 A_{\mathrm{s}}}{m_{\mathrm{s}}}, \tag{1.34}$$

where $\rho(r)$ is the dust density, $v_s(r)$ the velocity of the spacecraft with respect to the medium, A_s is its projected area in the direction of flight and m_s is its mass.

From a given value for the anomalous acceleration, the required density can be established. For the Pioneer spacecraft, with $A_s = 5.9$ m^2, $m_s = 241$ kg and $v_s = 11.8$ km/s, an acceleration $a_{\mathrm{Pio}} = 8.74 \times 10^{-10}$ m/s^2 results in a required density of $\rho = 2.48 \times 10^{-19}$ g/cm^3. This value is several orders of magnitude above known figures for interplanetary and interstellar dust densities, which are on the order of 10^{-24} g/cm^3 and 10^{-26} g/cm^3 respectively, as well as all the four considered Kuiper Belt models [4].
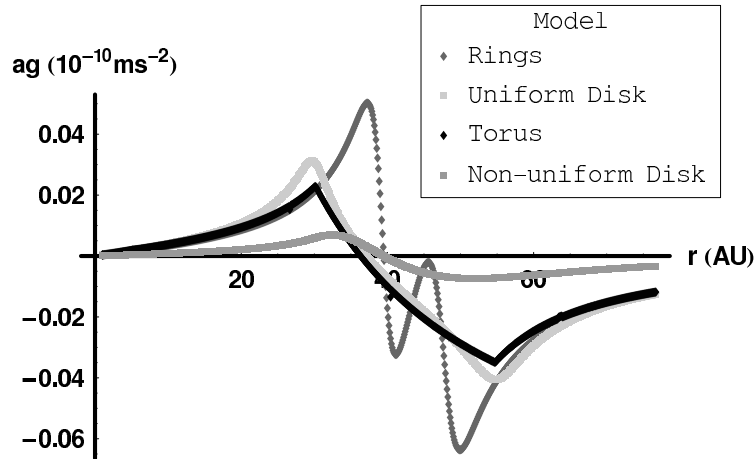
Figure 1.7: Gravitational acceleration acting on the Pioneer 10 for the Kuiper Belt models. The lighter grey represents the uniform disk, the medium grey the non-uniform disk, the dark grey the two-ring model and the black the torus model. Taken from Ref. [4].

1.2.3 Thermal Effects

As seen in Section 1.1.2, the initial estimate for the acceleration caused by thermal effects did not consider them a viable candidate to explain the anomaly [2]. However, these thermal effects quickly became controversial as other claims started to dispute the early estimates.

The first to suggest that the anomalous acceleration could be caused by thermal radiation effects was Murphy [13]. The main effect then considered was heat dissipation through the louvers that are built into the front of the main equipment compartment.

In a comment to the paper by Anderson *et al.* [2], Katz argues that the acceleration due to radiation from the RTGs may have been underestimated. The argument is based on the amount of waste heat available from the RTGs, evaluated at 2.11 kW, compared to the 85 W of a collimated beam necessary to account for the acceleration. Also, the author highlights the relevance of the electric heat dissipated from the front wall of the main equipment compartment [14].

The work carried out by Scheffer is a first attempt to combine the effects of heat radiated from the different sources onboard the spacecraft and provide an estimate of the global effect. The author isolates several distinct radiation sources and makes a series of considerations in order to compute their respective contributions. The obtained results are presented in terms of generated thrust and are summarised in Table 1.2 [6].

Table 1.2: Available thrust from different sources as of 1998 according to Scheffer's estimate. The last two rows represent the electrical power, that is expect to have a faster rate of decay than the radioactive heat sources due to thermocouple degradation, as explained in Ref. [6].

Source of Effect	Total Power (W)	Effic. (%)	Thrust (W)	Decay (%/year)
Rad from RHUs	8	0.5	4	0.78
Antenna shadow	25	0.3	7.5	0.68
Antenna radiate	25	0.6	15	0.68
RTG asymm.	2000	0.009	18	0.68
Feed pattern	0.8	0.7	0.6	0
Radio beam	7.2	−1	−7.2	0
Rad., main bus	59	0.54	32	see text in [6]
Rad., instr.	1	0.1	0.1	see text in [6]
Total			70	
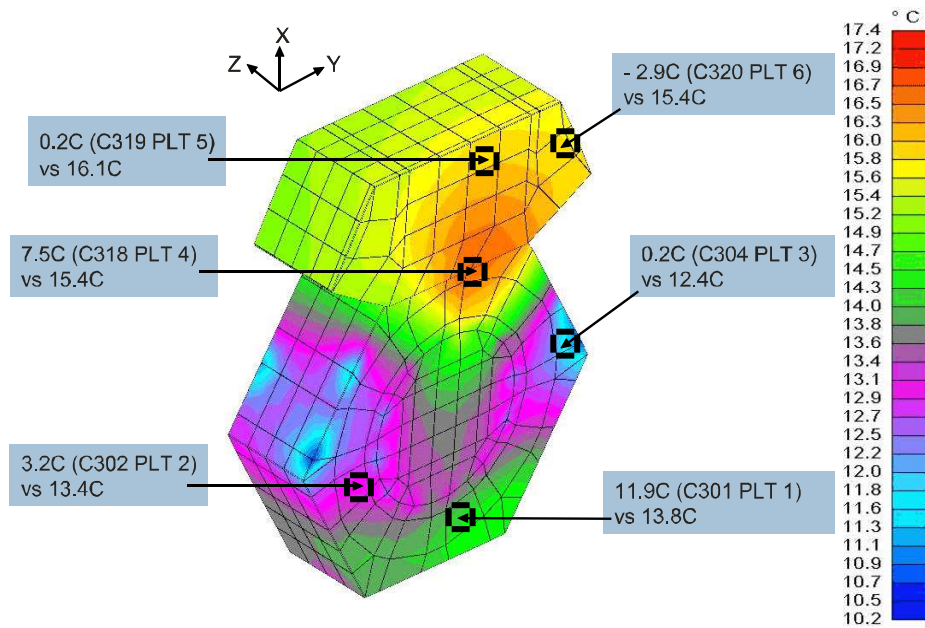
Figure 1.8: Preliminary temperature map of the outer surface of the Pioneer 10 spacecraft body, comparing temperatures calculated via a numerical finite element method vs. temperatures measured by temperature sensors, taken from Ref. [5].

Scheffer estimates that around $70\,W$ of directed power should be available, while only approximately $60\,W$ would be enough to account for the anomaly and, therefore, argues that thermal forces can explain the Pioneer Anomaly [6].

After these first rough estimates, some efforts to provide a more thorough and accurate study have been put in place. There are two teams with preliminary results already published. While Toth & Turyshev are yet to provide any force calculation, they put forward temperature maps obtained from a Finite Element Analysis (FEA) of internal heat conduction, such as the ones in Figs. 1.8 & 1.9. The purpose of these temperature maps is to calculate the surface temperature in order to obtain the radiated energy, given their emissivity [5].

The work presented in this dissertation was the first to present an estimate accounting for all the main effects. It also provides the framework for a thorough parametric study of the problem [10]. This constitutes an attempt to drift away from the full modelling of every engineering detail, and directs its attention to the physical basis of the probe's thermal behaviour.

In the mean time, Rievers *et al.* also published some preliminary force estimates using a simplified model of the RTGs and are working on a finite element model of the Pioneer [15]. Their results so far agree with the other available estimates, namely the one here presented [10].

Figure 1.9: Preliminary temperature map of one of the Pioneer 10 RTGs, taken from Ref. [5].

Chapter 2

Thermal Effects in Spacecraft

2.1 Radiative Momentum Transfer

Any surface exposed to electromagnetic radiation will be subject to a pressure due to that radiation. This fact was deduced theoretically by Maxwell in 1871 [16] and experimentally verified by Lebedev in 1900 (Ref. [17]) and by Nichols & Hull in 1901 [18]. This is the key phenomenon in play in an analysis of the thermal effects on a spacecraft's trajectory. Heat is emitted from the external surfaces as electromagnetic (infrared) radiation that carries a certain momentum and is absorbed and reflected by other surfaces. This section aims to provide the physical framework for this analysis.

Following the classic description of electromagnetism, the Poynting vector $\vec{S}$ is defined as the energy flux of the electromagnetic field and is given by

$$\vec{S} = \vec{E} \times \vec{H}, \tag{2.1}$$

where $\vec{E}$ is the electric field and $\vec{H}$ is the magnetic induction field. This relates to the energy density of the electromagnetic field

$$u_{\text{em}} = \frac{1}{2}\vec{E} \cdot \vec{D} + \frac{1}{2}\vec{H} \cdot \vec{B} \tag{2.2}$$

with $\vec{D}$ being the electric displacement and $\vec{B}$ the magnetic field. The Poynting Theorem

$$-\frac{\partial}{\partial t}u_{\text{em}} = \nabla \cdot \vec{S} + \vec{E} \cdot \vec{J}, \tag{2.3}$$

expresses the conservation of energy, where $\nabla \cdot \vec{S}$ gives the energy flux and the term $\vec{E} \cdot \vec{J}$ represents dissipation through Lorentz forces acting on charges ($\vec{J}$ is the current density). If we consider an electromagnetic wave propagating in a non-dissipative medium with direction $\vec{k}$, it can be shown that

$$\vec{H} = \sqrt{\frac{\varepsilon}{\mu}}\vec{k} \times \vec{E}, \tag{2.4}$$

where ε is the electric permitivity and μ is the magnetic permeability of the medium, from which follows

$$\vec{S} = v\,\vec{E} \cdot \vec{D}\,\vec{k} = v\,\vec{H} \cdot \vec{B}\,\vec{k}, \tag{2.5}$$

where v is the wave speed in the considered medium (in the vacuum $v = c$). Using Eq. 2.2, one obtains a relation between the energy flux of the electromagnetic wave and the energy density of the wave:

$$\vec{S} = v\,u_{\text{em}}\,\vec{k}. \tag{2.6}$$

It was shown by Maxwell that the pressure exerted on a surface exposed to an electromagnetic wave equals

$$P_{rad} = u_{\text{em incident}}. \tag{2.7}$$

This is valid for both incident and emitted radiation, since this represents a momentum transfer mechanism. Combining Eqs. 2.7 & 2.6 in the vacuum and taking into account the component normal to the illuminated surface, we finally obtain the relation between the energy flux and the radiation pressure

$$P_{rad} = \frac{\alpha}{c}\vec{S} \cdot \vec{n}, \tag{2.8}$$

where $\vec{n}$ is the surface normal. The parameter α is a radiation pressure coefficient that takes the value $\alpha = 1$ in the case of full absorption of incident radiation or simple emission. If there is reflection, the outgoing reflected wave will have an effect symmetric to the incident wave, in which case $1 < \alpha \leq 2$ (we can consider $\alpha = 1 + \rho$, where ρ is the reflection coefficient).

An alternative way to reach the same conclusion, is to use a quantum description, where electromagnetic energy is carried by discrete photons. The energy carried by a photon with a frequency ν_γ is given by

$$E_\gamma = h\nu_\gamma, \tag{2.9}$$

where h is Planck's constant. From Special Relativity, we know the relation between energy and momentum

$$E^2 = m_0^2 c^4 + p^2 c^2, \tag{2.10}$$

with p being the magnitude of the momentum and m_0 the rest mass, which for the photon is $m_{0_\gamma} = 0$. Therefore, it follows that

$$p_\gamma = \frac{E_\gamma}{c} = \frac{h\nu_\gamma}{c}. \tag{2.11}$$

If we consider a surface exposed to photons, the pressure exerted will be momentum transported per unit of time per unit of area. We can, therefore, write it in terms of the energy flux:

$$P_{rad} = \frac{1}{A}\frac{dp}{dt} = \frac{1}{A}\frac{\dot{E}}{c}. \tag{2.12}$$

In this case $\dot{E}$ is the energy of the photons hitting or leaving the surface. As before, in a reflection the force will be double of that of an absorbed or emitted photon of the same frequency. The relation in Eq. 2.12 is therefore equivalent to Eq. 2.8.

There is still a third way to reach the same relation by using the formalism of General Relativity, as done in Ref. [19].

2.2 Source Distribution Method

2.2.1 Motivation

As already discussed in the Section 1.1.2, the anomalous acceleration observed in the Pioneer trajectories is not fully and accurately characterised. In addition to that, the technical and engineering details about the spacecraft's design and construction are scattered across different sources of variable reliability and accuracy. Finally, the behaviour and evolution of the materials when exposed to the environment of space for over 30 years is unknown. This makes any reconstitution of this problem extremely difficult and, considering this, no definitive statements can be made about the origin of the Pioneer Anomaly.

The unavailability of detailed engineering specifications and schematics curtails the usefulness of a detailed Finite Element Analysis (FEA). In order to produce such an analysis, besides a detailed knowledge of the engineering details, the thermal behaviour of each component would have to be accurately modelled. In spite of this, there are at least a couple of these studies currently underway [5, 15]. These studies necessarily involve a large number of assumptions, compromising the reliability of the results.

For this analysis, there was an interest in using a method that would be computationally light, fast and flexible. This would allow for the results to be obtained without great computational resources or long processing time, providing for a quick evaluation of different scenarios. It is important to highlight the flexibility and speed of the method in coping with the scarcity of information and allowing for a sensitivity analysis that can identify the most important parameters. Another key issue is the scalability of the method, as it allows for the progressive construction of increasingly detailed models with growing precision, as the relative importance of the several contributions becomes evident.

The method chosen is based on a distribution of point-like radiation sources along the main emitting surfaces of the spacecraft and the analysis of how the emitted radiation is absorbed and reflected by other surfaces. This approach does not try to describe the behaviour of each internal component, but instead tries to capture the contributions of the main components of the spacecraft, namely the RTGs and the main equipment compartment. These contributions are derived from the global thermal and electrical power aboard the probes, which is reasonably well known.

There are some particular features of this problem that reinforce the choice for this particular approach. The temperature data is limited to the readings of six individual sensors inside the main compartment and two on the RTGs. That combined with the lack of knowledge about the optical properties of the used materials, especially after several decades in the space environment, introduce significant uncertainties, regardless of the adopted method. The approach here presented tries to base itself on the little solid and reliable data available.

It is emphasised that any study of this scope involves a large number of assumptions and hypotheses. Therefore, it is important to have the ability to quickly test a wide variety of scenarios and reach unambiguous conclusions about their plausibility. This sensitivity analysis is crucially facilitated by the short computation time of the present method. In addition, the simplicity of the formulation keeps the involved physics visible throughout the entire process, allowing for a close scrutiny of every step.

This approach, while less comprehensive than an FEA model, allows for a direct interpretation of results, easy adaptability, as well as rather short computation times.

Obviously, the self-consistency of the method should be assessed. Thus, before tackling the physical case of the Pioneer anomaly, a set of test cases was performed, as presented in Section 2.2.3. Furthermore, the choice for a point-like source approach should also be verified. This may be achieved by increasing the number of sources and observing the convergence of the relevant quantities and results. If deemed satisfactory, one may safely assume that continuous surfaces and components can be suitably modelled by point-like sources, so to still reproduce the physical interplay between them, and allow for an extrapolation to the Pioneer vehicles.

2.2.2 Formulation

The method chosen to tackle this problem is based on a distribution of isotropic and Lambertian point-like sources. An isotropic source is characterised by a uniform spherical power emission. If W is the emitted power, the time-averaged Poynting vector-field for an isotropic source located at (x_0, y_0, z_0) is given by

$$\vec{S}_{\text{iso}} = \frac{W}{4\pi} \frac{(x - x_0, y - y_0, z - z_0)}{[(x - x_0)^2 + (y - y_0)^2 + (z - z_0)^2]^{3/2}}. \tag{2.13}$$

In the case of a Lambertian source the optical intensity I of the radiation is constant along a hemisphere. Since the emitted power is given by the integration along a closed surface of the energy flux is

$$q = \int I \cos\theta \ d\omega = \int \frac{I}{r^2} \cos\theta \ dA, \qquad (2.14)$$

it follows that the energy flux is given by $(I/r^2)\cos\theta$. This results in a Poynting vector field where the flux is proportional to the cosine of the angle with the surface normal

$$\vec{S}_{\mathrm{Lamb}} = \frac{W \cos\theta}{\pi} \frac{(x - x_0, y - y_0, z - z_0)}{[(x - x_0)^2 + (y - y_0)^2 + (z - z_0)^2]^{3/2}}. \qquad (2.15)$$

Typically, isotropic sources are used to model point-like emitters and Lambertian sources to model surfaces. The Poynting vector field of the source distribution is, then, integrated over the exposed surfaces in order to obtain the amount of energy illuminating these and the force produced. The former is given by the time-averaged Poynting vector flux

$$E_{\mathrm{ilum}} = \int \vec{S} \cdot \vec{n} \ dA =$$
$$= \int \vec{S}(\vec{G}(s,t)) \cdot \left(\frac{\partial \vec{G}}{\partial s} \times \frac{\partial \vec{G}}{\partial t} \right) \ ds \ dt, \qquad (2.16)$$

where the function $\vec{G}(s,t)$ parameterises the relevant surface.

The radiation illuminating the surface will produce a force along the normal vector to that surface. Integrating that force, *i.e.*, the radiation pressure, given by Eq. (2.8), multiplied by the unitary normal vector, will give us the total force acting upon that surface. The same applies to the emitting surface itself. The force exerted upon it is the result of the integration of the pressure of the outgoing radiation field along a closed surface. In generic terms, the force due to radiation is given by

$$\vec{F}_{\mathrm{Rad}} = \int \frac{\vec{S} \cdot \vec{n}}{c} \frac{\vec{S}}{||\vec{S}||} \ dA. \qquad (2.17)$$

If the object in study has a reasonably complex geometry (such as the Pioneer spacecraft) there will be shadows cast by the surfaces that absorb and reflect the radiation. The shadowing effect of the illuminated surfaces is calculated with this same expression and then subtracted to the force obtained for the emitting surface. Alternatively, one may use an integration surface that encompasses the illuminated surfaces. The total result is the sum of all effects $\vec{F}_i$, force on the emitting surface, shadows and radiation pressure on the illuminated surfaces. We can then write an expression for the acceleration resulting from thermal effects:

$$\vec{a}_{\mathrm{Th}} = \sum_i \frac{\vec{F}_i}{m}. \qquad (2.18)$$

2.2.3 Test Cases

Before implementing this method and begin extracting results, it is sensible to conduct a series of test cases. The purpose is to assess the quality of the results and to gain sensitivity to the errors involved in the kind of approximations that are performed. The main issue is to ascertain if the radiation emitted from an extended surface can be adequately represented by a small number of point-like sources instead of a very fine mesh of radiating elements.

In these test cases, a $1 \ \mathrm{m}^2$ emitting surface is considered, with a second absorbing surface of similar size set at various distances and angles. These were chosen to be of the same order of magnitude as those of the particular problem in study. The radiation emissions are modelled with an increasingly finer mesh of point-like sources and results for the energy flux and force are then compared in a convergence analysis.

Table 2.1: Positions considered for the second surface in test cases. The first (emitting) surface is in the $0xy$ plane centred at the origin. Considered distances between both surfaces are typical for the Pioneer spacecraft.

Test Case #	Surface Centre Position (m)	Surface Tilt Angle (°)
1	$(2, 0, 0.5)$	90
2	$(2, 0, 1.5)$	0
3	$(2, 0, 1.5)$	30
4	$(2, 0, 1.5)$	60
5	$(2, 0, 1.5)$	90
6	$(1, 0, 2)$	0
7	$(1, 0, 2)$	30
8	$(1, 0, 2)$	60
9	$(1, 0, 2)$	90

Table 2.2: Results for Test Case 1 (*cf.* Table 2.1) considering a total emission of 1 W. As the number of sources to represent the thermal emission of a surface change, the resultant force components appearing by shadow on the secondary surface remain almost the same.

Sources #	Energy Flux (W)	Δ (%)	Force components (x, y, z) $(10^{-7}$ N$)$	Force intensity $(10^{-7}$ N$)$	Δ (%)
1	15.34		$(0.9300, 0, 0.1514)$	1.004	
4	15.92	3.8	$(1.028, 0, 0.1638)$	1.041	3.6
16	16.09	1.0	$(1.038, 0, 0.1675)$	1.051	0.98
64	16.13	0.26	$(1.040, 0, 0.1684)$	1.054	0.25
144	16.14	0.049	$(1.041, 0, 0.1686)$	1.054	0.047

For a single radiation emitting surface without any other illuminated surfaces, the force is normal to it and only depends on the total emitted power. Integrating Eq. (2.17) along a closed surface encompassing the emitting surface in the $0xy$ plane with Lambertian sources, we obtain a force pointing in the z-axis, of magnitude $(2/3)W_{\mathrm{surf}}/c$.

Computation of the shadow and radiation pressure on a second surface yields results that are not independent from the source distribution. In order to acquire some sensibility on that dependence, we plot the variation of the radiation intensity with the elevation and the azimuth for 1, 4, 16, 64 and 144 source meshes, as depicted in Figs. 2.1 and 2.2. These plots are obtained by integrating the energy flux along the azimuth or elevation to obtain its variation with elevation and azimuth, respectively.

A visual inspection of the results indicates that, even for the simpler 1 source mesh, the maximum deviation occurs at the higher angles of elevation and is less than 10%, when compared to the 144 source mesh. For the relevant angles for the Pioneer spacecraft configuration, deviations will be considerably smaller.

In order to confirm this assumption, the force acting on a second $1~\mathrm{m}^2$ surface for several different positions is computed. A total of nine configurations were considered, with different positions and tilt angles, as summarised in Table 2.1. The results are then computed for 1, 4, 16, 64 and 144 source meshes. The configurations were chosen to be representative of the typical dimensions and angles involved in the geometric configurations of the kind of spacecraft in question, in particular, the Pioneer probes. The full results for the energy flux and force components for each test case are presented in Tables 2.2 to 2.10.

Of all the analysed cases, the highest deviation occurs for Test Case 8, confirming previous expectations, since the second surface is set at high elevation from the emitting surface, as depicted in Fig. 2.3. The results in Table 2.9 show a difference of approximately 6% between the force obtained with one source and the results for the finer meshes (16, 64 and 144 sources). Nevertheless, the latter are all within 0.5% of each other, and the intermediate 4 source mesh has a deviation of under 1.5% to the 144 source mesh.
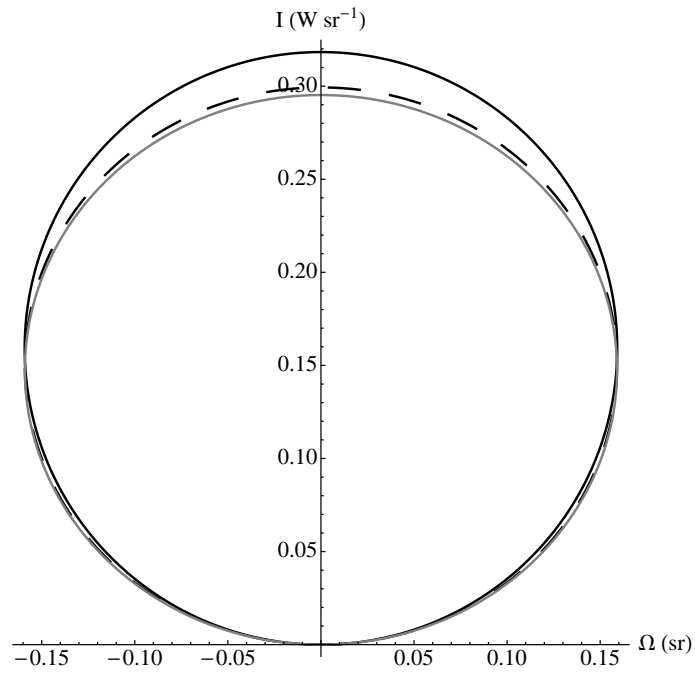
Figure 2.1: Polar plot of the energy flux variation with elevation of the radiation emitted by a surface on the $0xy$ plane (solid angle Ω), when considering 1, 4 and 16 Lambertian sources (full, dashed and grey curves, respectively), maintaining the total emitted power constant at $1\ \mathrm{W}$ (the curves for 64 or 144 sources overlap the one for 16 sources). The intensity at higher elevations (close to vertical) diminishes with the number of sources, compensating the slight increase at the lower angles.

Figure 2.2: Same as Fig. 2.1, but for intensity variation with azimuthal angle θ. All lines are superimposed, confirming that the total power is maintained constant.

Table 2.3: Same as Table 2.2, for Test Case 2.

Sources #	Energy Flux (W)	Δ (%)	Force components (x, y, z) $(10^{-7}$ N$)$	Force intensity $(10^{-7}$ N$)$	Δ (%)
1	19.20		$(0.4952, 0, 1.037)$	1.149	
4	19.83	3.3	$(0.5032, 0, 1.082)$	1.192	3.8
16	19.99	0.80	$(0.5050, 0, 1.093)$	1.204	0.92
64	20.03	0.20	$(0.5054, 0, 1.096)$	1.207	0.23
144	20.04	0.036	$(0.5055, 0, 1.096)$	1.207	0.042

Table 2.4: Same as Table 2.2, for Test Case 3.

Sources #	Energy Flux (W)	Δ (%)	Force components (x, y, z) $(10^{-7}$ N$)$	Force intensity $(10^{-7}$ N$)$	Δ (%)
1	26.13		$(1.110, 0, 1.292)$	1.703	
4	26.13	0	$(1.111, 0, 1.320)$	1.725	1.3
16	26.13	0	$(1.111, 0, 1.327)$	1.731	0.314
64	26.13	0	$(1.111, 0, 1.329)$	1.732	0.076
144	26.13	0	$(1.111, 0, 1.329)$	1.732	0.014

Table 2.5: Same as Table 2.2, for Test Case 4.

Sources #	Energy Flux (W)	Δ (%)	Force components (x, y, z) $(10^{-7}$ N$)$	Force intensity $(10^{-7}$ N$)$	Δ (%)
1	44.41		$(2.416, 0, 1.646)$	2.923	
4	44.41	0	$(2.409, 0, 1.663)$	2.928	0.14
16	44.41	0	$(2.407, 0, 1.668)$	2.928	0.027
64	44.41	0	$(2.407, 0, 1.669)$	2.929	0.0059
144	44.41	0	$(2.406, 0, 1.669)$	2.929	0.0011

Table 2.6: Same as Table 2.2, for Test Case 5.

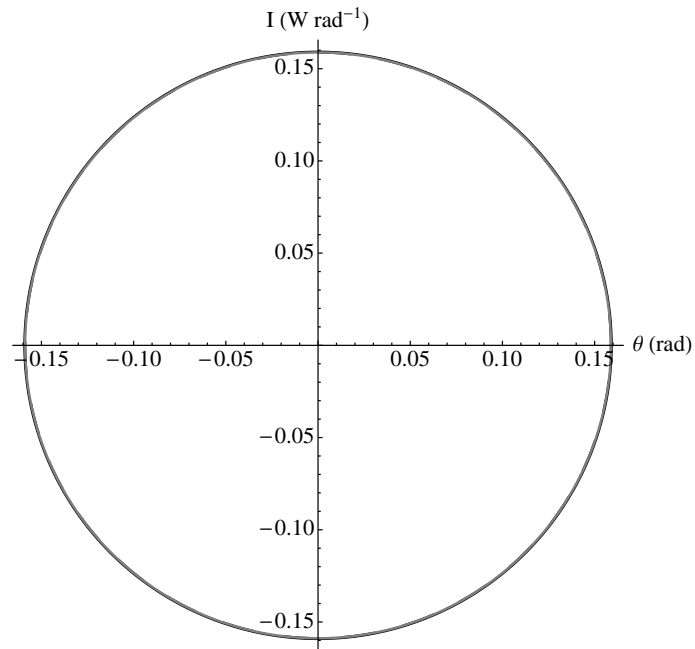| Sources #	Energy Flux (W)	Δ (%)	Force components (x, y, z) $(10^{-7}$ N$)$	Force intensity $(10^{-7}$ N$)$	Δ (%)
1	23.25		$(1.395, 0, 0.4525)$	1.467	
4	23.25	0	$(1.383, 0, 0.4581)$	1.457	0.68
16	23.25	0	$(1.379, 0, 0.4593)$	1.454	0.21
64	23.25	0	$(1.378, 0, 0.4596)$	1.453	0.055
144	23.25	0	$(1.378, 0, 0.4597)$	1.453	0.010

Table 2.7: Same as Table 2.2, for Test Case 6.

Sources #	Energy Flux (W)	Δ (%)	Force components (x, y, z) $(10^{-7}$ N$)$	Force intensity $(10^{-7}$ N$)$	Δ (%)
1	49.52		$(0.6818, 0, 3.130)$	3.203	
4	49.52	0	$(0.6306, 0, 3.060)$	3.124	2.4
16	49.52	0	$(0.6190, 0, 3.042)$	3.104	0.63
64	49.52	0	$(0.6161, 0, 3.037)$	3.099	0.16
144	49.52	0	$(0.6156, 0, 3.036)$	3.098	0.029

Table 2.8: Same as Table 2.2, for Test Case 7.

Sources #	Energy Flux (W)	Δ (%)	Force components (x, y, z) $(10^{-7}$ N)	Force intensity $(10^{-7}$ N)	Δ (%)
1	50.36		$(1.574, 0, 2.938)$	3.333	
4	50.36	0	$(1.501, 0, 2.855)$	3.225	3.2
16	50.36	0	$(1.484, 0, 2.834)$	3.199	0.81
64	50.36	0	$(1.480, 0, 2.829)$	3.193	0.20
144	50.36	0	$(1.479, 0, 2.828)$	3.191	0.037

Table 2.9: Same as Table 2.2, for Test Case 8.

Sources #	Energy Flux (W)	Δ (%)	Force components (x, y, z) $(10^{-7}$ N)	Force intensity $(10^{-7}$ N)	Δ (%)
1	45.53		$(2.016, 0, 2.083)$	2.899	
4	45.53	0	$(1.918, 0, 2.003)$	2.773	4.3
16	45.53	0	$(1.895, 0, 1.984)$	2.744	1.1
64	45.53	0	$(1.890, 0, 1.979)$	2.736	0.27
144	45.53	0	$(1.889, 0, 1.978)$	2.735	0.050

Table 2.10: Same as Table 2.2, for Test Case 9.

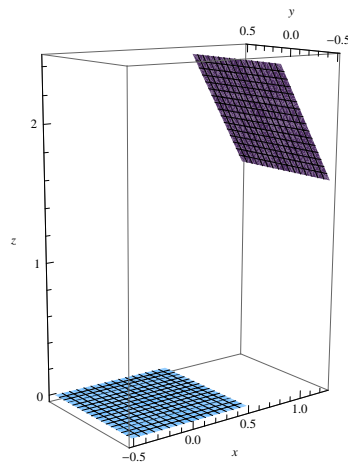| Sources #	Energy Flux (W)	Δ (%)	Force components (x, y, z) $(10^{-7}$ N)	Force intensity $(10^{-7}$ N)	Δ (%)
1	24.29		$(1.305, 0, 0.6316)$	1.450	
4	24.29	0	$(1.251, 0, 0.6113)$	1.393	4.0
16	24.29	0	$(1.238, 0, 0.6059)$	1.378	1.0
64	24.29	0	$(1.235, 0, 0.6045)$	1.375	0.26
144	24.29	0	$(1.234, 0, 0.6043)$	1.374	0.048

Figure 2.3: Geometry of Test Case 8 (*cf.* Table 2.1): thermal emission from a surface is simulated by a different number of Lambertian sources evenly distributed on the surface, maintaining the total emitted power constant, and the effect on a second surface is observed. This is the test case where the highest variation with the number os sources considered were obtained.

Table 2.11: Results for the surface feature test case where the impact of ignoring a cubic shape placed on top of a flat surface is analysed. The total power is kept constant at $1\,\mathrm{W}$ and the temperature is assumed uniform in all surfaces. The deviations Δ with respect to the plane surface without any features are small enough to allow this simplification.

Feature height (cm)	Force intensity ($10^{-6}\,\mathrm{N}$)	Δ (%)
0	2.224	
1	2.223	0.040
5	2.202	1.0
10	2.139	3.9

Table 2.12: Results for the corner fillet test case with a constant total power of $1\,\mathrm{W}$. The deviation Δ of the force intensity with respect to the sharp corner are kept within reasonable values.

Fillet dimension (cm)	Force components (x, y, z) ($10^{-7}\,\mathrm{N}$)	Force intensity ($10^{-7}\,\mathrm{N}$)	Δ (%)
0	$(1.112, -1.112, 0)$	1.573	
1	$(1.115, -1.115, 0)$	1.577	0.2
5	$(1.129, -1.129, 0)$	1.596	1.5
10	$(1.146, -1.146, 0)$	1.620	3.0
20	$(1.181, -1.181, 0)$	1.670	6.2

For the typical angles of the Pioneer probe's configuration, one may take as figure of merit Test Cases 1 and 3. For the first case, depicted in Fig. 2.4, the radiation pressure and shadow yield the results shown in Table 2.2. The analysis of these results shows that, for 16, 64 and 144 sources, the variation in the energy flux and force is less than 0.5%. In addition to that, the difference to the finer meshes is less than 5% for 1 source and less than 1.5% for a 4 source mesh. The results in Table 2.4 show, for Test Case 3, a variation of less than 5% between the results for 1 source and 144 sources. The convergence is, as in both previous cases, achieved for the 16, 64 and 144 source meshes, with a variation of less than 0.25%.

For all test cases examined, the convergence of the results occurs at a similar pace and yields similarly small deviations. Ultimately, we conclude that a 4 source mesh, with deviations around 1.5%, is adequate for the desired balance between precision and simplicity. These results provide a fairly good illustration of the power of the proposed method and how well we can estimate the radiation effects on the Pioneer probes. In particular, the deviation is always well below 10%, even with the roughest simplifications allowed by the chosen method. We may then conclude that, for the scales and geometry involved in a thermal model of the Pioneer, the source distribution method is, not only consistent and convergent, but that it provides a very satisfactory estimate of the thermal radiation effects, considering all uncertainties involved.

Finally, after analysing the convergence of the method, we also considered two additional test cases aiming to assess the effect of ignoring minor surface features, such as the equipment attached to the external walls of the spacecraft and other geometric details. The two particular situations analysed were a cubical piece on top of a $1\,\mathrm{m}^2$ plane surface, as shown in Fig. 2.5, and two perpendicular surfaces with a fillet (a "cut corner"), as in Fig. 2.6. In each case, the force resulting from the emissions of the surfaces was compared. The total power is kept constant and the temperature is assumed uniform in all surfaces.

The results presented in Tables 2.11 & 2.12 set boundaries on the kind of geometric simplifications that can be made without a significant impact in the final result and keeping in line with the targets of precision set for this study.

These results indicate that, in the absence of large temperature gradients, no significant errors will arise from considering flat surfaces and not taking into account all the details of the spacecraft.

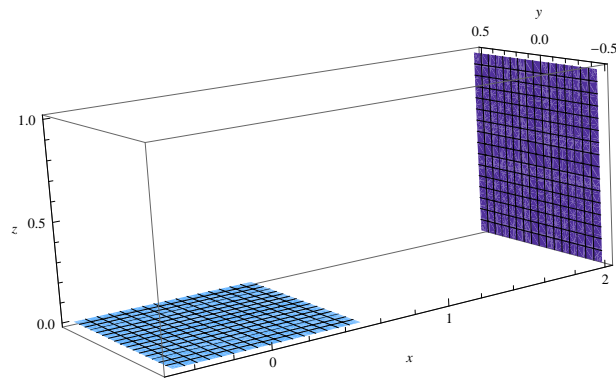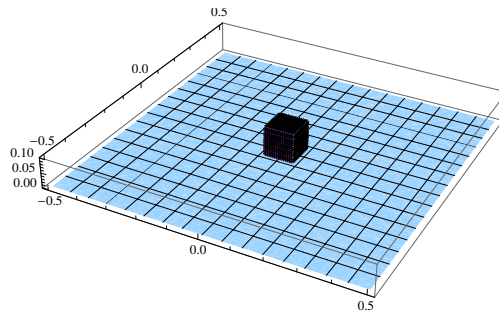Figure 2.4: Same as Fig. 2.3, for Test Case 1.

Figure 2.5: Geometry for the surface features test case. A cubical shape is placed on top of the flat surface and the force is compared for different sizes of this cube, while the total power is kept constant.
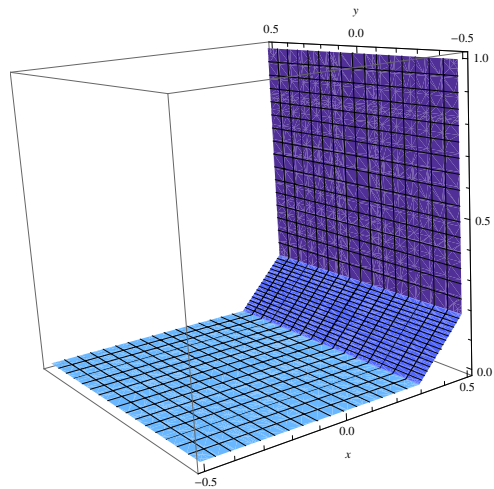

Figure 2.6: Geometry for the corner fillet test case. The results are compared while the dimension of the fillet varies and the total power is kept constant.

Chapter 3

Thermal Study of the Pioneer Anomaly

3.1 Thermal Model of the Pioneer Spacecraft

3.1.1 Geometry

The construction of an accurate geometric model of the Pioneer can be a rather involved and difficult job. The lack of detailed information on the specifications and constructive parameters further complicates this task.

However, this problem can be made considerably easier with some sensible simplifications. The first and most important of all resides on the fact that these probes are spin stabilised with its axis of rotation coincident with the axis of the parabolic high-gain antenna. Furthermore, it is assumed they are in a steady-state thermal equilibrium during the relevant part of the journey. These assumptions allow one to discard the time-averaged radial components of radiation, as their effect will cancel over each complete rotation of the probe.

In addition to that, the probe's antenna and axis of rotation are pointing approximately towards Earth, which is also the approximate direction of the detected anomalous acceleration. This direction is here defined as the z-axis. This problem is, thus, reduced to quantifying the force caused by radiation anisotropies in the axial or z direction, allowing one to consider a simplified geometric model of the spacecraft.

The model built for this study includes only the most important features of the Pioneer spacecraft, namely, the main parabolic antenna, the main equipment compartment behind it and the two Radioisotope Thermoelectric Generators (RTGs).

The main antenna is a paraboloid with a diameter of 2.77 m and 0.48 m deep . It can be parameterised in cartesian coordinates by $G_{\mathrm{ant}}(s,t) = (s, t, a(s^2 + t^2))$ with $a = 0.25$ m^{-1}. The separation between the back of the antenna and the main equipment compartment is 0.19 m The main equipment compartment is an hexagonal prism 0.343 m deep and with 0.66 m long sides. The model for these two components is depicted in Fig. 3.1.

The two RTGs have cylindrical shapes with 6 fins and are connected to the main compartment by 3 m long trusses. Fig. 3.2 shows a schematic of the model with all the considered components.

In this model, radiation sources are distributed along the main equipment compartment and the RTGs, which represent the main sources of thermal power aboard the spacecraft. The emissions are then integrated along the visible portion of the antenna and equipment compartment.

The surface of this compartment facing the antenna is discarded since most radiation emitted from this wall or reflected through the antenna itself will have a radial contribution and its effect on the final result will be negligible. In addition to that, the antenna's temperature will be very low with an approximately uniform distribution between its front and back surfaces. Therefore, its contribution can be regarded as negligible when compared to other components, with the surface acting solely as a reflector for the incoming radiation.
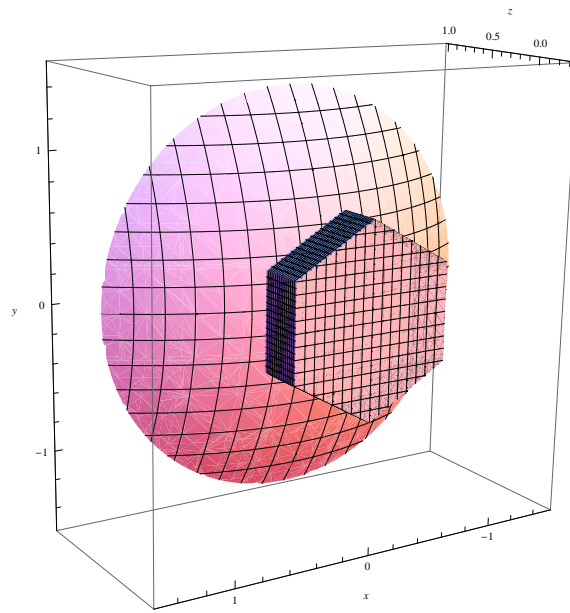
Figure 3.1: Back view of the Pioneer spacecraft model geometry considered in calculations: high gain antenna and hexagonal main bus compartment.
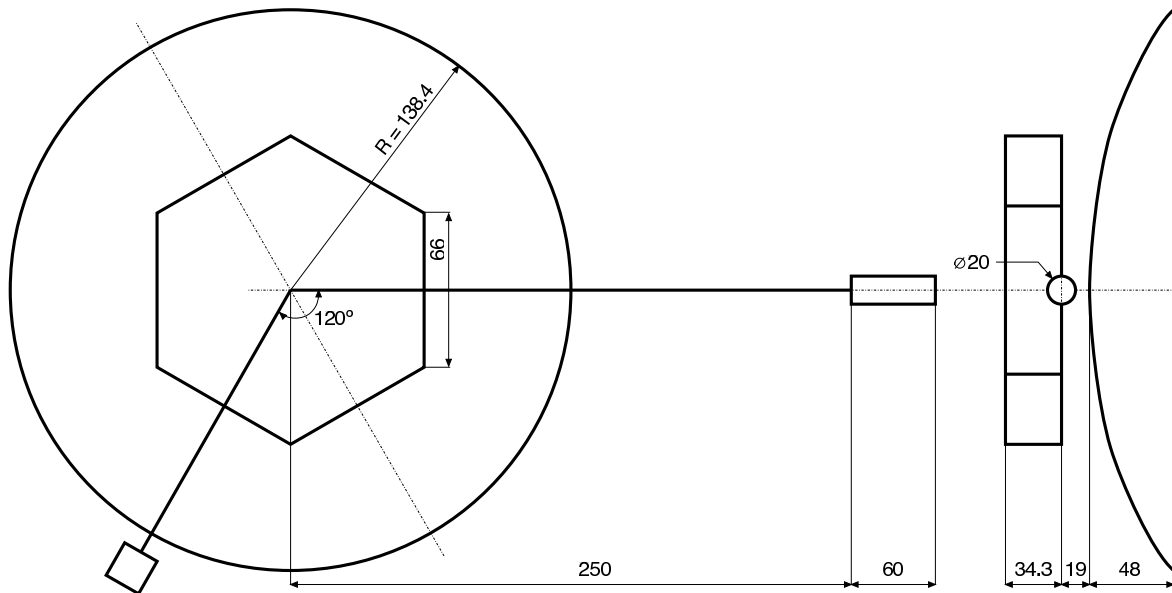

Figure 3.2: Schematics of our simplified model of the Pioneer spacecraft, with relevant dimensions in cm (second RTG and truss are not represented to scale, for convenience). Lateral view indicates the relative position of the RTGs, box compartment and the gap between the latter and the high gain antenna.

This simplified configuration captures the most important contributions to the thermal reaction force, since the RTGs and main compartment are responsible for the vast majority of emitted power.

3.1.2 Source Distribution

In order to perform the thermal analysis of the Pioneer spacecraft, the three main contributions in play are addressed separately.

The main equipment compartment is thermally controlled through the Multi-Layer Insulation (MLI) that covers it and a series of louvers located in the front of the spacecraft (defined here as the wall facing away from the Sun). The louvers are controlled through a bimetallic spring joint that opens or closes them according to the temperature.

The front wall of the probe (the one facing away from the Sun), where the heat dissipating louvers are located, is perpendicular to the probe's axis of rotation. Since there are no other walls or objects to reflect or absorb the radiation emitted from the front, its contribution to the thermal recoil force will only be dependent on the emitted power. Assuming Lambertian emitters, after integration of the Poynting vector field using Eq. (2.17) the force in the z-axis will be given by

$$F_{\text{front}} = \frac{2}{3}\frac{W_{\text{front}}}{c}. \tag{3.1}$$

The contribution from the side walls of the main compartment is obtained from the integration of the shadow and radiation pressure components along the antenna, according to the methodology presented in Section 2.2.2. The shadow of the RTGs is neglected since they are small, relatively distant, and most of its effect would be in the radial direction. Following an approach similar to the one used in the test cases, in order to verify the convergence of the result, the integration was performed for an increasing number of sources assuming a uniform surface temperature, *i.e.* all point-like sources have the same power. This convergence analysis is summed up in Table 3.1.

Table 3.1: Results of the convergence analysis on the thermal contribution of the side wall of the main equipment compartment with uniform surface temperature. W_{lat} is the power emitted from the 6 side walls of the main equipment compartment.

Sources #	Force in z-axis (N)	Δ (%)
1	$0.1727(W_{\text{lat}}/c)$	
2	$0.1715(W_{\text{lat}}/c)$	0.68
3	$0.1709(W_{\text{lat}}/c)$	0.34
4	$0.1684(W_{\text{lat}}/c)$	1.4
8	$0.1688(W_{\text{lat}}/c)$	0.18

The results are all close to each other, with deviations always below 1.5%, confirming the consistency previously demonstrated in our test cases. The obtained values show that between 16.8% to 17.3% of the power emitted from the side walls of the compartment is converted into a Sun-ward thrust along the z-axis.

It is also important to verify how the results are affected by a non-uniform temperature distribution. This is simulated by varying the relative power of the point-like sources in each surface, keeping the total power attributed to the surface constant. A variation of 20% in power between sources (simulating a 5% temperature variation) gives no significant changes in the final result, with relative differences smaller than 1%.

It should also be mentioned that the MLI covering the equipment compartment should limit the temperature gradient along the main external surfaces (except in special places, *e.g.*, the louvers, that can be modelled as separate sources if required) and render the modelling of many of the details of the compartment unnecessary
.

Taking this analysis into account, a mesh with 4 sources in each one of the side walls is chosen to model the main equipment compartment. This choice is made in the belief that it presents a good balance between the accuracy of the results and the desired simplicity and computational speed. We also argue that considering a uniform temperature along this wall is a reasonable simplification with a small effect in the final result. Finally, due to the symmetry of the model, only one of the six side walls needs to be analysed, since all other five will have the same contribution.

The contribution of the RTGs can be computed through two different models.

The first, simpler scenario, considers each RTG as a single isotropic source. In this case, the point-like source has the whole power of the RTG (W_{RTG}) yielding a direct contribution of

$$F_{\mathrm{RTG}} = 0.01856 \frac{W_{\mathrm{RTG}}}{c}. \tag{3.2}$$

In the second model, the cylindric shape of the RTG is taken into account and a Lambertian source is placed at each base. Actually, it is only necessary to consider the radiation source facing towards the centre of the spacecraft, as the remaining RTG radiation will be emitted radially and its time-averaged contribution vanishes. In this case, the Lambertian source has a portion of the total RTG power proportional to the surface area it represents. In terms of the power emitted from the RTG base facing the central part of the probe (W_{RTGb}), the force becomes

$$F_{\mathrm{RTG}} = 0.1277 \frac{W_{\mathrm{RTGb}}}{c}, \tag{3.3}$$

which is equivalent to approx. 2% of total RTG power, if the temperature is considered uniform.

These results have been confirmed by preliminary figures for the RTG contribution published by Rievers *et al.* [15].

3.1.3 Power Budget

In this study, it was decided from the outset to use the power instead of the temperature as the independent variable from which all estimates are derived. Besides being physically more consistent, the available data is more reliable. Actually, it is one of the few relevant parameters that is reasonably well known from the mission data.

The analysis is carried out based on the energy balance of the spacecraft

$$\dot{E}_{\mathrm{absorb}} + \dot{E}_{\mathrm{gen}} = \sum_i A_i \epsilon_i \sigma T_i^4, \tag{3.4}$$

where $\dot{E}_{\mathrm{absorb}}$ is the power absorbed from the medium (negligible, in this case), $\dot{E}_{\mathrm{gen}}$ is the power generated onboard and T_i is the temperature of the surface i with an area A_i and an emissivity ϵ_i.

If we were to use the temperature as an input, since the optical properties and their evolution with time are not well known, a solution would have to be obtained iteratively for each set of assumed optical properties. Otherwise, it would result in a violation of the conservation law in Eq. (3.4) or in a disagreement with the more reliable power data.

The two plutonium-238 RTGs are responsible for all the power that is generated onboard the probe. These RTGs use a mass of plutonium as a heat source to generate electricity through a set of thermocouples. Their power conversion efficiency is around 5%, the remaining power being dissipated as thermal radiation through the external walls and fins of the RTGs themselves. The fraction of power that is converted into electricity is used to power all the spacecraft systems.

There is certainly some heat conduction through the truss from the RTG to the central compartment. However, given the small section of this structure, it is reasonable to admit that it will have a reduced impact
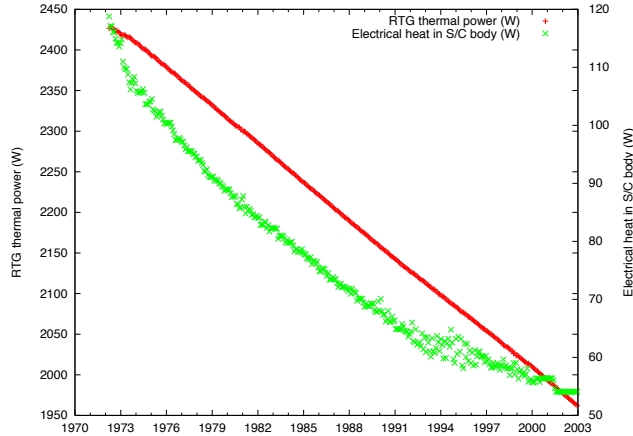
Figure 3.3: Heat generated by RTGs (red) and electrical equipment (green) over the lifetime of Pioneer 10, taken from Ref. [5].

on the total RTG radiated power (a quick estimate, assuming the RTGs trusses as hollow cylinders, with radius of 1 cm and a temperature gradient of 30 K/m, we obtain less than 4 W of conducted power, which is clearly negligible). It is thus assumed at this stage that all of the RTG thermal power is dissipated as radiation from the RTG itself.

According to Ref. [2], the total RTG thermal power at launch was 2580 W. Taking into account the decay of plutonium-238 with a half-life of 87.74 years, the total onboard power would follow the exponential law

$$W_{\text{tot}}(t) = 2580 \ e^{\left(-\frac{t \ln 2}{87.74}\right)} \ [\text{W}].\tag{3.5}$$

Telemetry reveals, however, that electrical power decay is actually much faster than this, probably due to the degradation of the thermocouples. The available data shows that the heat from electrical equipment in the spacecraft body decays from about 120 W just after launch to less than 60 W in the later stages of the mission, as exemplified in Fig. 3.3 . This decay approximately follows an exponential law with a half life of about 24 years [5].

3.2   Results

3.2.1   Order of Magnitude Analysis

To begin the study of thermal effects in the Pioneer probes, it is useful to undertake some rough order of magnitude calculations in order to acquire some sensibility to the kind of values involved.

To perform this analysis, one takes values from the spacecraft specifications and power estimates. Thus, the spacecraft mass is taken as $m_{\text{Pio}} \sim 230$ kg, while the RTG and equipment compartment thermal power are, respectively, $W_{\text{RTG}} \sim 2$ kW and $W_{\text{equip}} \sim 100$ W.

Considering the simpler model presented in Section 3.1.2, with point-like RTGs and hexagonal equipment compartment, with uniform surface temperature and emissivity in each component, an estimate of the force generated in the axial direction can be obtained:

$$F_{\text{RTG}} \sim 2 \times 10^{-2} \frac{W_{\text{RTG}}}{c},$$
$$F_{\text{sides}} \sim 10^{-1} \frac{W_{\text{equip}}}{c},$$
$$F_{\text{front}} \sim 2 \times 10^{-1} \frac{W_{\text{equip}}}{c}. \tag{3.6}$$

Taking the spacecraft mass into account, one can easily obtain a first estimate for the acceleration arising from thermal power dissipation in the RTGs and main equipment compartment

$$a_{\text{RTG}} \sim 2 \times 10^{-2} \frac{W_{\text{RTG}}}{m_{\text{Pio}}\, c} \sim 6 \times 10^{-10} \text{ m/s}^2,$$
$$a_{\text{equip}} \sim 3 \times 10^{-1} \frac{W_{\text{equip}}}{m_{\text{Pio}}\, c} \sim 4.4 \times 10^{-10} \text{ m/s}^2. \tag{3.7}$$

This analysis already yields the relevant result that neither the contribution from the RTGs or the instrumentation are negligible and they both have similar orders of magnitude, in agreement with a previous estimate [6]. Furthermore, the resulting estimate for the acceleration has a similar magnitude to the Pioneer anomaly $a_{\text{Pio}} \sim 10^{-9}$ m/s^2, providing additional motivation to proceed with a more detailed study of these effects.

3.2.2 Thermal Force Estimate

The results of the analysis performed in Section 3.2.1 encourage us to proceed and attempt to obtain a more accurate estimate of the thermal effects using the point-like source distribution method outlined in Section 2.2.2.

In order to achieve the desired balance between simplicity and accuracy, a model with 4 point-like Lambertian sources in each side wall of the main equipment compartment and a Lambertian source at each base of the RTG was chosen for this analysis, as described in Section 3.1.2. The deviation of this model to the finer meshes considered is less than 0.5%, when considering uniform temperature in each wall. It is also worthwhile to remind that a temperature difference of 5% along the surface of the side wall would yield changes smaller than 1% in the contribution to the thermal acceleration.

The computation performed with this model allows one to extract an expression for the thermal acceleration

$$a_{\text{Th}} = \frac{0.168 W_{\text{sides}} + \frac{2}{3} W_{\text{front}} + 0.128 W_{\text{RTGb}}}{c\, m_{\text{Pio}}} \tag{3.8}$$

that only depends on the total emitted power from the front wall W_{front}, side wall W_{sides} and the RTG base facing the centre of the spacecraft W_{RTGb}.

A critical analysis of this expression, bearing in mind the spacecraft geometry, reveals that all considered contributions yield a Sun-ward acceleration. The W_{front} component radiates directly in a direction away from the Sun, while the other two components W_{sides} and W_{RTGb} radiate laterally, illuminating the high gain antenna, yielding a significant shadow and radiation pressure.

The question now lies in correctly estimating each one of these powers. We shall consider the 1998 readings, as found in Fig 3.3, namely $W_{\text{RTG}} = 2050$W and $W_{\text{equip}} = 58$W. These are the dissipated thermal powers at the RTG and equipment compartment.

The simplest scenario, with uniform temperature and optical properties (emissions proportional to the surface area), leads to
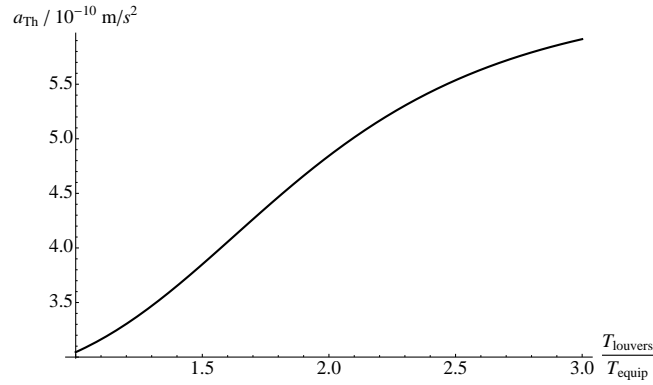
Figure 3.4: Variation of the resulting acceleration with the temperature ratio between the louvers and the equipment platform, considering similar emissivities for both multi-layer insulations.

$$W_{\text{sides}} = 21.75 \text{ W},$$
$$W_{\text{front}} = 18.12 \text{ W},$$
$$W_{\text{RTGb}} = 41.11 \text{ W}, \tag{3.9}$$

yielding an acceleration $a_{\text{Th}} = 3.05 \times 10^{-10}$ m/s^2. This accounts for around 35% of the anomalous acceleration. However, a critical analysis of this figure, considering the available temperature maps [19], tells us that the temperature anisotropies along the sides of the equipment compartment fall within the tested cases discussed in Section 3.1.2. However, the RTG temperature distribution should deserve further attention, as there are significant temperature changes between the lateral wall of the cylinder, the bases and the fins. In addition, it is expected that the front wall of the equipment compartment will have a larger contribution than the side walls, due to the presence of the louvers.

Taking this into account, one should analyse the variation of the emitted power in the louvers and at the base of the RTGs, since these are the two critical parameters in the calculation. If one considers that the louvers are closed and have a similar emissivity to the rest of the equipment platform, one can plot the variation of the acceleration with the temperature ratio between the louvers and the mean temperature of the platform, while keeping the total power constant. This is depicted in Fig. 3.4. We can perform a similar analysis for the RTGs, considering the ratio between the temperatures at the base of the cylinder and the fins (Fig. 3.5).

Figs. 3.4 and 3.5 illustrate of the main strength of the chosen method: it allows for a quick graphical analysis of the dependence of the final result on specific parameters. Through Eq. (3.8) and sensible variation of the power parameters, we can match temperature readings and consider hypotheses for the variation of the optical properties.

We can now perform a second estimate considering the RTG cylinder bases and wall as having a 15% and 30% higher temperature than the fins, respectively. Assuming also that the closed louvers have similar emissivities, although a 100% higher temperature than the rest of the equipment compartment could be possible, we obtain the following values for the powers:
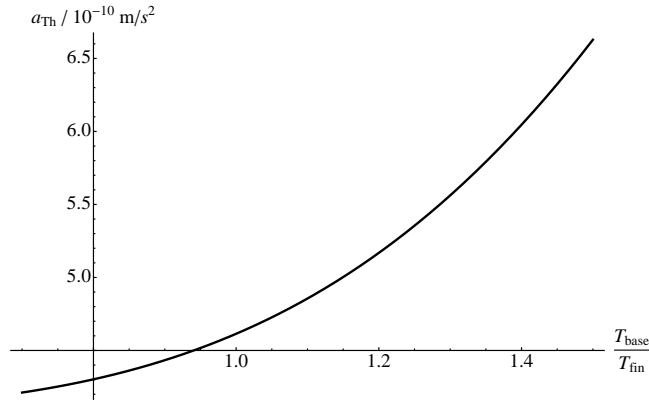
31

Figure 3.5: Variation of the resulting acceleration with the temperature ratio between the base of the RTG cylinder and the fin temperature.

$$
\begin{aligned}
W_{\text{sides}} &= 9.97 \text{ W}, \\
W_{\text{front}} &= 39.71 \text{ W}, \\
W_{\text{RTGb}} &= 49.67 \text{ W}.
\end{aligned}
\tag{3.10}
$$

In this case, we can account for 57% of the anomalous acceleration, that is, $a_{\text{Th}} = 5.00 \times 10^{-10} \text{ m/s}^2$.

The results presented so far do not consider reflections, *i.e.*, full absorption of the radiation by the illuminated surfaces. In this study, we can introduce diffusive reflection by assigning a value to the α parameter in Eq. (2.8). For the kind of aluminium used in the construction of the antenna, the reflectivity is, typically, around 80% for the relevant wavelengths, yielding $\alpha = 1.8$. For the multi-layer insulation of the equipment platform, a value of $\alpha = 1.7$ is considered. In these conditions, the illumination factors in Eq. (3.8) are modified to account for the reflection. With the same temperature conditions as in the previous case, the resulting acceleration is $a_{\text{Th}} = 5.75 \times 10^{-10} \text{ m/s}^2$, approximately two thirds of the anomalous acceleration.

3.2.3 Discussion

The results presented in the previous section give us a fairly good idea of the changes involved when considering different hypotheses and parameters. The three scenarios here discussed illustrate how our method can be used to identify the most sensitive parameters and quickly assess the effect of the existing uncertainties, pointing to the necessary refinements to improve the reliability of the results.

At this stage it is also important to highlight some of the limitations of the methodology used to obtain the results so far.

First of all, some simplifications were assumed when building the geometric model of the Pioneer spacecraft, necessarily introducing some errors. However, as discussed in Section 3.1.1, these simplifications keep the most important features of the spacecraft. Also, given the lack of detailed blueprints and construction details, it would be extremely difficult and not necessarily worthwhile to undergo a very accurate modelling.

The second important limitation is the lack of a complete model for reflection. Only diffusive reflection is taken into account in a very simple manner through the radiation pressure parameter α in Eq. (2.8).

On the other hand, the computational package used to perform the calculations as a very high numerical

32

integration accuracy. The error estimates provided by the software are on the order of 10^{-14}, while the approximation of the geometry with point-like sources results in an expected deviation of less than 1%.

It is also relevant to point out the transparency of the method, as well as the battery of test cases presented that provide for a close scrutiny of all the performed calculations.

Despite the consistency of the method used, the mentioned limitations will motivate future refinements and improvements that can increase the accuracy and reliability of the results. Given all this, the findings presented here constitute the first systematic and credible engineering approach to the thermal effects on the Pioneer Anomaly to be able to produce a complete set of results for this problem.

Chapter 4

Conclusions & Outlook

We began this discussion by presenting the initial detection of the Pioneer Anomaly and data recovery process, as well as the assessment of all known systematic effects. In these first estimates by Anderson *et al.*, the thermal effects contribution to the acceleration was evaluated at $(0.55 \pm 1.88) \times 10^{-10}$ m/s^2, excluding them from the set of possible explanations [2].

The controversy raised around the importance of the thermal contribution made the importance of the study here presented quite obvious. It constitutes the first quantitative and systematic effort to address this issue and present results that include all the main contributions.

The first relevant conclusions are indicated by the order of magnitude analysis in Section 3.2.1. It is then confirmed that, not only are the contributions from the RTGs and electrical equipment both relevant, but they have a similar importance. Furthermore, the order of magnitude of their combined effects is, in this first rough estimate, comparable to that of the Pioneer anomalous acceleration. This consolidates previous claims that addressed these contributions separately [13, 14, 6] and establishes the thermal effects as a viable candidate for the cause of the anomaly.

The results presented in Section 3.2.2 are fairly robust, as they are based on the methodology developed throughout this dissertation that was subject to a battery of test cases before being judged able to perform the desired calculations. One thus reiterates the confidence in the estimates provided by the source-distribution method.

The three situations under analysis show that, so far, between 35% and 67% of the Pioneer Anomaly can be attributed to thermal radiation momentum transfer. This shows that these effects were underestimated by, at least, an order of magnitude as compared to the initial evaluation. This implies that a thermal explanation for the Pioneer Anomaly is becoming the most likely scenario.

Bearing that in mind, it should be noted that the figures presented here are not, by any means, final or definite. They still have a high degree of variability that is mainly related to the way the emitted power is distributed along the different surfaces and point-like sources and the optical properties of those surfaces.

In this context, this work has an obvious path ahead in an attempt to refine the currently available results. This refinement will necessarily involve improvements to the geometric model and the development of a physical model that takes into account both diffusive and specular reflection. These improvements should be always guided by the same objectives that were present from the onset, maintaining the speed, flexibility and transparency of the method.

It should also be kept in mind that there are important limitations to any approach to this problem, namely the scarcity of data about the engineering details of the Pioneer spacecraft, limited and imprecise measurements from the onboard sensors and, most importantly, the lack of an unequivocal characterisation of the Pioneer Anomaly itself. It is useful to remind that these limitations were the main motivation for the choice of method adopted in this study.

Finally, the most important contribution of this task should be a thorough parametric study of the main parameters involved. This is crucially facilitated by the architecture of the method, as already demonstrated here by the sample of scenarios considered and analysed. This dissertation is presented in the conviction that this analysis is an important contribution to the understanding of the Pioneer Anomaly.

Bibliography

[1] NASA - The Pioneer Missions. URL: `http://www.nasa.gov/centers/ames/missions/archive/pioneer.html`.

[2] John D. Anderson, Philip A. Laing, Eunice L. Lau, Anthony S. Liu, Michael Martin Nieto, and Slava G. Turyshev. Study of the anomalous acceleration of Pioneer 10 and 11. *Physical Review D*, 65(8):082004, Apr 2002.

[3] J. R. Brownstein and J. W. Moffat. Gravitational solution to the Pioneer 10/11 anomaly. *Classical and Quantum Gravity*, 23(10), 2006.

[4] O. Bertolami and P. Vieira. Pioneer anomaly and the Kuiper Belt mass distribution. *Classical and Quantum Gravity*, 23(14):4625–4635, 2006.

[5] Viktor T. Toth and Slava G. Turyshev. Pioneer Anomaly: Evaluating Newly Recovered Data. In Alfredo Macias, Claus Lammerzahl, and Abel Camacho, editors, *RECENT DEVELOPMENTS IN GRAVITATION AND COSMOLOGY: 3rd Mexican Meeting on Mathematical and Experimental Physics*, volume 977, pages 264–283. AIP, 2008.

[6] Louis K. Scheffer. Conventional forces can explain the anomalous acceleration of Pioneer 10. *Physical Review D*, 67(8):084021, Apr 2003.

[7] John D. Anderson, Philip A. Laing, Eunice L. Lau, Anthony S. Liu, Michael Martin Nieto, and Slava G. Turyshev. Indication, from Pioneer 10/11, Galileo, and Ulysses Data, of an Apparent Anomalous, Weak, Long-Range Acceleration. *Physical Review Letters*, 81(14):2858–2861, Oct 1998.

[8] Craig B. Markwardt. Independent Confirmation of the Pioneer 10 Anomalous Acceleration. arxiv.org/gr-qc/0208046, 2002.

[9] Viktor T. Toth. Independent Analysis of the Orbits of Pioneer 10 and 11. *International Journal of Modern Physics D*, 18(5):717–741, 2009.

[10] O. Bertolami, F. Francisco, P. J. S. Gil, and J. Páramos. Thermal analysis of the Pioneer anomaly: A method to estimate radiative momentum transfer. *Physical Review D*, 78(10):103001, 2008.

[11] O. Bertolami and J. Páramos. The Pioneer anomaly in the context of the braneworld scenario. *Classical and Quantum Gravity*, 21(13):3309–3321, 2004.

[12] J. W. Moffat. Scalar–tensor–vector gravity theory. *Journal of Cosmology and Astroparticle Physics*, 03(004), 2006.

[13] Edward M. Murphy. Prosaic Explanation for the Anomalous Accelerations Seen in Distant Spacecraft. *Physical Review Letters*, 83(9):1890, Aug 1999.

[14] J. I. Katz. Comment on "Indication, from Pioneer 10/11, Galileo, and Ulysses Data, of an Apparent Anomalous, Weak, Long-Range Acceleration". *Physical Review Letters*, 83(9):1892, Aug 1999.

[15] Benny Rievers, Stefanie Bremer, Meike List, Claus Lämmerzahl, and Hansjörg Dittus. Thermal dissipation force modeling with preliminary results for Pioneer 10/11. *Acta Astronautica*, 06(009), 2009.

[16] James Clerk Maxwell. *A Treatise on Electricity and Magnetism*. Clarendon Press, Oxford, 1873.

[17] P. Lebedev. Untersuchungen über die Druckkräfte des Lichtes. *Annalen der Physik*, 1901.

[18] E.F Nichols and G.F. Hull. The Pressure due to Radiation. *The Astrophysical Journal*, 17(5):315–351, 1903.

[19] Viktor T. Toth and Slava G. Turyshev. Thermal recoil force, telemetry, and the Pioneer anomaly. *Physical Review D*, 79(4):043011, 2009.